Orthotropic viscoelastic characterization of thin woven composites by a combination of experimental and numerical methods

Gautier Girard, Marion Martiny, Sébastien Mercier

Orthotropic viscoelastic characterization of thin woven composites by a combination of experimental and numerical methods

Gautier Girard*, Marion Martiny, Sébastien Mercier

Université de Lorraine - CNRS - Arts et Métiers ParisTech, Laboratoire d'Etude des Microstructures et de Mécanique des Matériaux, 7 rue Félix Savart 57070 Metz, France

Abstract

Electric mobility is the driving force for the development of power electronic devices embedded in printed circuit boards (PCBs). Fast charge of batteries generates large increase of temperature in PCBs. Therefore, the characterization of the thermo-viscoelastic behavior of laminates is a necessity. Tests have been conducted at elevated temperature, with a specific attention to minimize the oxidation of the material. To model precisely the viscoelastic response of the laminate, since pure resin samples are usually not available, an inverse method based on the comparison of experimental results and finite elements simulations is proposed. Periodic boundary conditions allowing to apply uniaxial tension with an arbitrary orientation are developed. In order to validate this method, resin samples are extracted from pre-impregnated material and tested under the same temperature conditions. In a last step, the cyclic response of a buried hole in a PCB is simulated by finite element calculations, using the identified material data. For large maximum temperature, substantial differences are highlighted between thermo-elastic and thermo-viscoelastic approaches in terms of accumulated plastic strain in the copper barrel. The present work opens new possibilities to model the lifetime of electronic devices facing temperature excursions ranging over the glass transition temperature.

Keywords: woven composite, viscoelasticity, orthotropic behavior, numerical homogenization, thermal cycles, printed circuit boards

1. Introduction

As part of the energy transition, electronic devices play a central role. Therefore, Printed Circuit Boards (PCBs), which are the main carrier of electronic components, are at the heart of many studies and new developments. In the fields of electric mobility or aerospace, PCBs are subjected to significant thermal loads and a precise characterization of the thermo-mechanical behavior of the materials that constitute them is pivotal in order to predict their lifetime. Most of the insulating materials used in PCBs are composites made of glass fibers and a thermosetting polymer matrix, whose mechanical behavior is highly dependent of temperature and time. Consequently, the mechanical behavior of the composite is itself time- and temperature-dependent. The assessment of the mechanical response of the composite is of interest for the simulation of PCB assemblies, especially for plated through hole [1, 2] or embedded components reliability [3].

These thin materials show an orthotropic mechanical response due to their glass fiber reinforcement. Mechanical measurements are only easily achievable in the plane of the weaving pattern. Thus, an homogenization procedure is often adopted to evaluate the orthotropic behavior of woven composite materials, knowing the matrix and glass fiber behaviors and the internal microstructure of the composite. For linear elasticity, many authors proposed a homogenization method (Barbero et al. [4], Green et al. [5], Chen et al. [6], Girard et al. [7]) in which the behaviors of the yarns are obtained by a first homogenization and used later for the homogenization at the woven composite level.

The same method of two-scale homogenization is usually applied to obtain the viscoelastic behavior at the woven composite level. Zhu et al. [8] carried out the viscoelastic homogenization of a woven composite substrate for printed circuit boards. The viscoelastic behavior of the epoxy matrix was taken from the literature and was modeled with a Prony series. At the yarn level, micro-mechanical relations based on the self-consistent scheme have been used to obtain the viscoelastic response. At the woven composite level, a finite element model was used. Kwok and Pellegrino [9] have identified the viscoelastic behavior of the epoxy matrix and then applied finite element method (FE) at both homogenization stages in order to find the macroscopic viscoelastic behavior of the composite. Xu et al. [10] used a similar approach to predict the homogenized behavior of a woven composite for different fiber contents. Courtois et al. [11] characterized an epoxy resin at various temperatures and degrees of cure. Based on experiments, a degree of cure- and temperature-dependent mechanical model was proposed for the resin. The model was further adopted in [12], where the 3D homogenization of the viscoelastic behavior of a woven composite was presented. The same model was used by Benavente et al. [13] to predict the geometrical deformation of a L-shaped composite part during its manufacturing. By applying the Laplace-Carson (LC) transform to the viscoelastic material, a linear relation between strains and stresses

*Corresponding author

Email address: gautier.girard@univ-lorraine.fr (Gautier Girard)

in Laplace space was found. An elastic homogenization was performed in the Laplace space and an inverse LC transform led to the homogenized viscoelastic behavior in the time space. The Laplace Carson transform is adopted to determine the viscoelastic response of composite materials since decades. One can mention the pioneering work of Hashin [14] who proposed the solution of the Eshelby problem (an inclusion embedded into an infinite matrix) for incompressible linear viscoelastic phases. When the relaxation stiffness is described by a Prony series with N constituents, Hirsekorn et al. [15] finally needed $N+3$ elastic homogenizations to obtain the homogenized viscoelastic behavior. These three additional steps were necessary to ensure a good conditioning of the inverse LC transform. Recently, Hirsekorn et al. [16] extended their numerical model to determine the effective time-dependent thermal expansion coefficients of the unit cell as the result of the time and temperature dependency of a viscoelastic matrix. In their approach, the expansion coefficients of the local phase (glass fiber and resin) were assumed time independent.

The present paper focuses on the characterization of the thermo-viscoelastic behavior of a woven composite used in PCBs. Relaxation tests are performed in the plane of the material and the out of plane properties (that cannot be measured by experiments) are obtained by numerical homogenization. The identified behavior is later used in the simulation of a buried via to observe the effect of the thermal loading on the lifetime of the PCB. The experimental measurements made on the composite material are presented in section 2. Master curves are deduced from these measurements and the corresponding shift functions are determined. Section 3 recalls the viscoelastic constitutive model, based on Prony series. Following the idea of Courtois et al. [11], an original spectrum equation describing the relaxation moduli is proposed. The numerical model is presented in section 4 with a precise geometrical characterization of the RVE proposed through scanning electron microscope (SEM) images. To model the viscoelastic behavior of a thin woven composite, a two-scale homogenization method based on finite elements is presented. While LC and inverse LC were needed in Hirsekorn et al. [15], here the two-stage homogenization is performed directly in the time domain. In the present work, the behavior of the resin is not known a priori, so an inverse method is needed. As the main outcome of our work, the homogenized response of the woven composite is obtained together with the viscoelastic response of the resin. Resin samples could be extracted from pre-impregnated material, allowing for an experimental validation. The main advantage of the inverse method lies in the fact that it can be applied even when resin samples cannot be manufactured. In a last section, the obtained behaviors of the woven composite and resin are introduced in a FE simulation of a buried via in a PCB subjected to thermal loads. Viscoelastic effects on the lifetime prediction of the structure are analyzed by comparing the results to the elastic case.

2. Relaxation tests

The considered material is a laminate used in the PCB industry, made of a thermoset epoxy type resin with $180\,^{\circ}\mathrm{C}$ T_g , reinforced by a 2116 plain weave glass fabric. In this section, the experimental procedure is detailed. Relaxation tests are performed with a specific attention paid to prevent oxidation of the samples at elevated temperature.

2.1. Experimental procedure

Dogbone specimens of total length $84\,\mathrm{mm}$ (gauge length of $50\,\mathrm{mm}$) and width $15\,\mathrm{mm}$ have been cut in the considered laminate by contour milling performed by the PCB manufacturer CIMULEC, following the standards of PCB manufacturing. Copper layers are present on both ends of the sample to prevent it from slipping off the grips during the test, see the geometry presented on the left part of Figure 1. The thickness of specimens has been measured precisely on SEM images, leading to a mean value of $99.5\,\mu\mathrm{m}$ with a standard deviation of $1.4\,\mu\mathrm{m}$. A speckle pattern of paint is sprayed on the samples and strain measurements are carried out by digital image correlation (DIC). 3 megapixel images of the central area of the sample are taken all along the test. They are divided in subsets of size 51 pixels, with a step size of 17 pixels. The computed strains are observed to be homogeneous and the overall strain is computed by averaging over the whole central area of the sample. The tensile machine Instron E3000 available at the LEM3 platform is used, equipped with a thermal chamber (Instron 3119-605 Temperature controlled chamber) and a $\pm 250\,\mathrm{N}$ load cell (Instron Dynacell 2527-131).

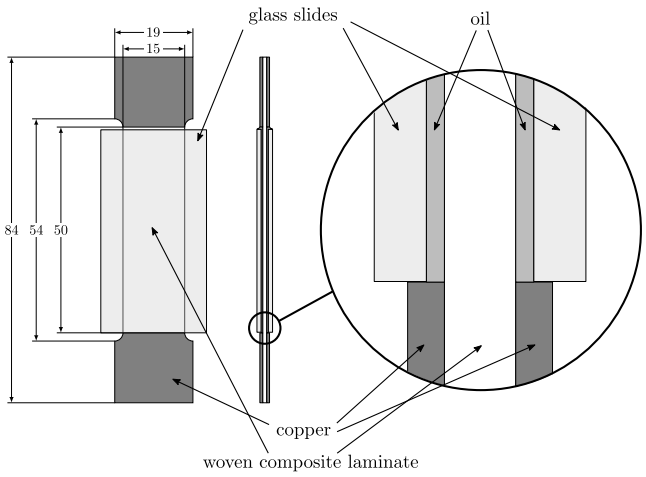

Figure 1: Sample used for relaxation tests: front view, side view and zoom on the side view. Oil and glass slides avoid the occurrence of oxidation.

First, a preconditioning of the material is adopted with a temperature excursion at $190\,^{\circ}\mathrm{C}$ for $2\,\mathrm{h}$. This stage has a threefold goal: ensuring that the cure of the resin is complete, drying the sample and removing any internal stresses. The heating of the chamber is then switched off for more than $3\,\mathrm{h}$ so that the device and sample are steady at room temperature. The specimen is then subjected to a series of relaxation tests at different temperatures; a constant strain is applied while the load evolution is recorded. The first temperature plateau is set to $40\,^{\circ}\mathrm{C}$.

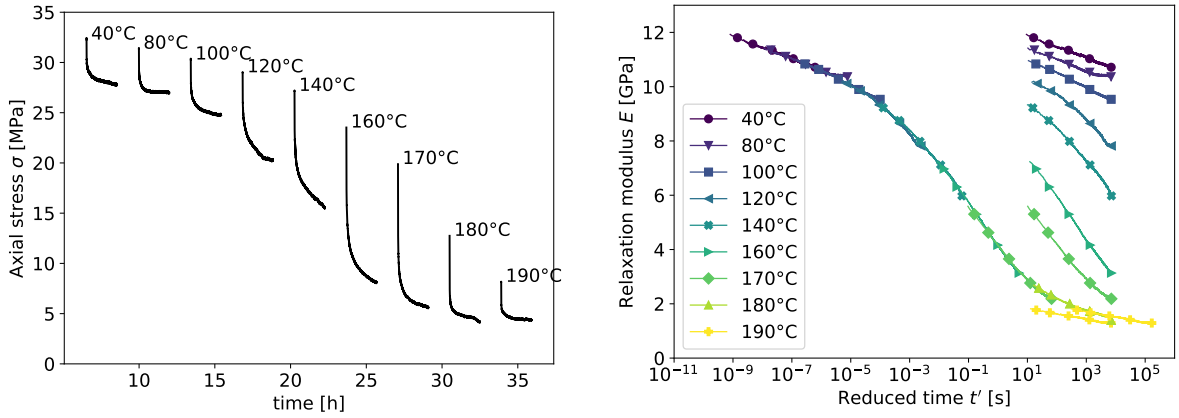

(a) (b)

Figure 2: (a) Axial stress measured during a series of relaxation tests on one sample. (b) Relaxation modulus $E(t)$ measured for each temperature plateau and master curve obtained by shifting the original responses along the time axis.

A time period of 75 min is dedicated to the temperature stabilization of the whole system. Next, a displacement of 0.12 mm is applied to the specimen and held for 2 h, to measure the relaxation behavior. Afterwards, the load is released to 1 N and the temperature is raised to the new level. The procedure is repeated on each specimen for the nine selected temperatures : 40, 80, 100, 120, 140, 160, 170, 180 and 190 °C.

It has been observed that the mechanical response changes when the complete relaxation tests is repeated several times on the same sample without any protective layers. The sample changes color: from originally yellow, it darkens with each test. This change in color is therefore associated to a modification of the physical state of the material due to oxidation.

In the PCB industry, all operations at large temperature are made in an environment with a lack of oxygen. For instance, during hot pressing, the laminates are pressed under low vacuum. In addition, when exposed to large temperature during their lifetime, PCBs are protected from oxygen by a varnish. In contrast, here the tests were executed in presence of air and are not relevant from realistic situations. The oxidation of these composite materials is well documented in the literature. Polansky et al. [17, 18] and Lé-Magda et al. [19] worked on the evolution of the glass transition temperature with oxidation and material aging on FR4 materials. Gigliotti et al. [20] developed a material constitutive behavior integrating the thermo-oxidation effect for this type of material. However, the aim is here to eliminate this phenomenon since it is not observed during the lifetime of PCBs that we are investigating. A simple experimental setup has therefore been developed, see Figure 1. A thin film of sunflower oil is deposited on the sample surface to protect it from any contact with oxygen. The sunflower oil has been chosen because it has a smoke point above 200 °C. As the sample is tested vertically, the oil would eventually flow out, so two glass slides for use in microscopy are placed on both sides of the sample. They stick by capillarity with the oil and are supported down by the shoulder made by the copper layers present at the extremities of the sample (see Figure 1). The speckle pattern is not affected by oil or heat and the transparency of the oil and of the glass slides still enables the use of DIC for strain measurements without any noticeable image distortion or without affecting the speckle pattern. To ensure that the oil and glass slides have no effect on the strain measurement, a tensile test has been made with glass slides and oil only on some part of the sample. The field of view was adjusted to observe the sample with protection on half of the image and without protection on the other half. A displacement step was applied for a duration of 75 s and 200 images were taken. The axial strain is computed by DIC and the average value on the protected side and on the bare side gave coincident strain measurements.

It has been checked that this setup prevents efficiently the oxidation effects on the samples during relaxation tests up to 200 °C. Two consecutive tests on the same sample showed indeed repeatable results.

2.2. *Experimental results*

The strains in the plane are measured by DIC and confirm the application of a constant longitudinal strain during each relaxation step. The strain step is applied in less than 10 s. The amplitude of the strain applied is approximately 0.25 %, the exact value being measured continuously for each test. From the load evolution, the stress is computed (Figure 2a) and the relaxation modulus is computed as $E(t) = \sigma(t)/\varepsilon$, where the longitudinal strain ε represents the measured value over each loading interval. The relaxation response is obtained for each temperature plateau, as seen on the right part of Figure 2b. These nine curves (in the range [10; 7200]s) will be employed next to compose the master curve.

Three samples have been tested for each of the three orientations 0°, 45° and 90°, following the procedure presented in section 2.1. The results obtained on one sample in the 45° direction are presented on Figure 2. Figure 2a shows that the measured stress is reduced for higher temperature plateaus. The relaxation modulus $E(t)$ obtained for each temperature plateau are shown in Figure 2b. The time-temperature superposition

principle allows for obtaining a master curve by shifting the relaxation responses on the logarithmic time scale. The master curve of the same experiment is shown on Figure 2b and covers a time range of more than 15 decades (between 10^{-10} s and 10^{5} s). The glass transition temperature has been chosen as the reference temperature here: $T_{ref} = T_g = 180\,^{\circ}\mathrm{C}$. The linear viscoelastic hypothesis was verified by testing 45° samples under strain amplitudes of $0.125\,\%$, $0.25\,\%$ and $0.5\,\%$, always obtaining an identical response $E(t)$.

Figure 3a presents all master curves for the nine tests. A good repeatability of the experiments is depicted for the three orientations. Indeed, for each direction, the three curves corresponding to three tests are almost superimposed. One can notice a stiffer response in the 90° orientation as compared to 0°, and a much softer response for 45°.

The shift factors used to construct the 9 master curves of Figure 3a are plotted on Figure 3b. Very close shift factors are obtained for all samples for temperatures between $100\,^{\circ}\mathrm{C}$ and $180\,^{\circ}\mathrm{C}$. Some discrepancy is observed below $100\,^{\circ}\mathrm{C}$ and for $190\,^{\circ}\mathrm{C}$. It does not seem to be associated to the orientation, but may rather be explained by experimental dispersion. The relaxation curve is rather flat at low temperatures and a small error on the measured force or strain may lead to large variations on the shift factor. At $190\,^{\circ}\mathrm{C}$, the relaxation curve also approaches a plateau, moreover the oil is close to its smoke point and its viscosity may start to change, thus affecting the results. Nevertheless, the consistency of the measurements for the nine tests enforces the idea that the shift factor is not orientation dependent.

3. Viscoelastic constitutive model

3.1. Model formulation

As observed in Figure 3a, the mechanical behavior of laminates used in PCB is strongly dependent on time and temperature and is next modeled with the theory of linear viscoelasticity. The Boltzmann superposition integral is adopted to model the 3D viscoelastic response, as proposed elsewhere and recently for laminates [9, 15]:

$$\boldsymbol{\sigma}(t) = \int_0^t \underline{\boldsymbol{C}}(t-s) : \frac{\boldsymbol{d\varepsilon}(s)}{ds}\, ds \tag{1}$$

with $\underline{\boldsymbol{C}}(t)$ the time dependent relaxation stiffness tensor. Bold notation indicates second order tensors, bold and underlined notation, fourth order tensors. The double dot product denotes contraction over two indices.

In this work, the viscoelastic model will be used to describe the response of the resin (matrix assumed isotropic), the yarns (assumed transversely isotropic) and the woven composite (assumed orthotropic). In case of orthotropic behavior and using Voigt notation, $\underline{\boldsymbol{C}}(t)$ reads:

$$\underline{\boldsymbol{C}}(t) = \begin{bmatrix} C_{11}(t) & C_{12}(t) & C_{13}(t) & 0 & 0 & 0 \\ C_{12}(t) & C_{22}(t) & C_{23}(t) & 0 & 0 & 0 \\ C_{13}(t) & C_{23}(t) & C_{33}(t) & 0 & 0 & 0 \\ 0 & 0 & 0 & C_{44}(t) & 0 & 0 \\ 0 & 0 & 0 & 0 & C_{55}(t) & 0 \\ 0 & 0 & 0 & 0 & 0 & C_{66}(t) \end{bmatrix} \tag{2}$$

Nine independent components are necessary to describe $\underline{\boldsymbol{C}}(t)$ in the case of an orthotropic material. The number of independent terms is reduced to five for materials with a transverse isotropic behavior (e.g. the yarns of the studied composite), and two in the isotropic case (e.g. the resin).

In the present work, $\underline{\boldsymbol{C}}(t)$ is written in terms of a Prony series :

$$\underline{\boldsymbol{C}}(t) = \underline{\boldsymbol{C_\infty}} + \sum_{k=1}^{N} \underline{\boldsymbol{C_k}} \mathrm{e}^{-t/\tau_k} \tag{3}$$

Here, $\underline{\boldsymbol{C_\infty}}$ is the long-term relaxation stiffness tensor and $\underline{\boldsymbol{C_k}}$ are the Prony coefficients tensors associated to the relaxation times τ_k. Note that the instantaneous stiffness tensor $\underline{\boldsymbol{C_0}}$ is given by :

$$\underline{\boldsymbol{C_0}} = \underline{\boldsymbol{C_\infty}} + \sum_{k=1}^{N} \underline{\boldsymbol{C_k}} \tag{4}$$

For an orthotropic behavior, there are $9(N+1)$ material parameters. The stress tensor can thus be written as:

$$\boldsymbol{\sigma}(t) = \underline{\boldsymbol{C_\infty}} : \boldsymbol{\varepsilon}(t) + \sum_{k=1}^{N} \underline{\boldsymbol{C_k}} : \boldsymbol{q_k}(t) \tag{5}$$

The tensorial internal variables $\boldsymbol{q_k}(t)$ associated with each τ_k called history variables [21], are written as :

$$\boldsymbol{q_k}(t) = \int_0^t \mathrm{e}^{-(t-s)/\tau_k} \frac{\boldsymbol{d\varepsilon}(s)}{ds}\, ds \tag{6}$$

3.2. Relaxation moduli distribution

The components of the relaxation stiffness tensor can be expressed in a dimensionless form:

$$c^{ij}(t) = \frac{C^{ij}(t)}{C_0^{ij}} \tag{7}$$

where C_0^{ij} are the components of the instantaneous stiffness tensor. The Prony series expansion of the dimensionless relaxation stiffness tensor components writes:

$$c^{ij}(t) = 1 - \sum_{k=1}^{N} c_k^{ij} (1 - \mathrm{e}^{-t/\tau_k}) \tag{8}$$

with $c_k^{ij} = C_k^{ij}/C_0^{ij}$ the dimensionless Prony coefficients. Since $0 \leq C_\infty^{ij} \leq C_0^{ij}$, one can write:

$$0 \leq \frac{C_\infty^{ij}}{C_0^{ij}} = 1 - \sum_{k=1}^{N} c_k^{ij} \leq 1 \tag{9}$$

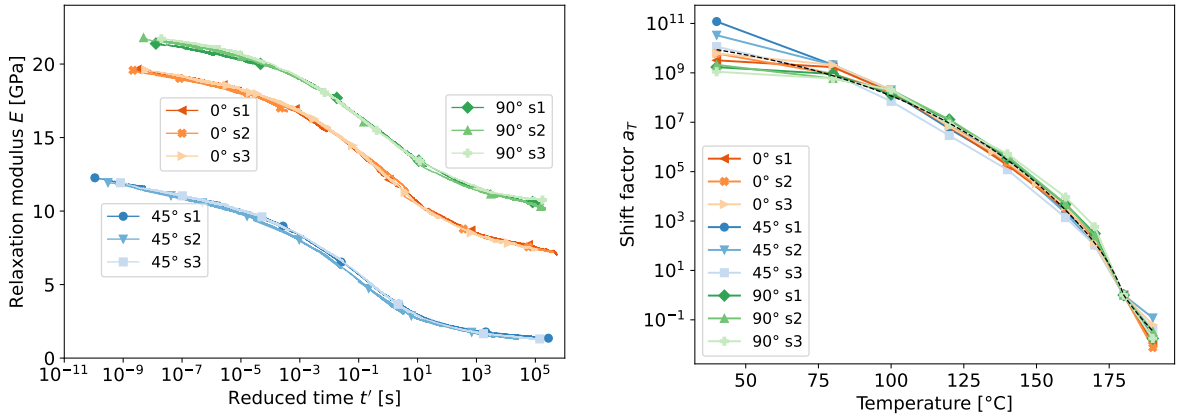

(a) (b)

Figure 3: (a) Master curves obtained for each test on the studied composite at orientations 0°, 45° and 90°. Three tests have been performed for each orientation. (b) Shift factors a_T identified to obtain the master curve. The discontinuous black line represents the shift function (18) fitted to the data.

or equivalently,

$$0 \leq \sum_{k=1}^{N} c_k^{ij} \leq 1 \tag{10}$$

It is often seen in the literature that one relaxation time per decade is required to describe the relaxation functions correctly. Over wide ranges of time and temperature, N can become large and $N+1$ Prony coefficients per components of $\underline{\boldsymbol{C}}(t)$ have to be identified. For that purpose, Courtois et al. [11] proposed a continuous function, named spectrum equation, describing the evolution of the Prony coefficients C_k^{ij} with the relaxation times τ_k. The continuous function they used consists of the sum of a Gaussian and a sigmoid. However, depending on the function parameters, the inequality (10) may not always be satisfied. This can be problematic during the automatic optimization stage, for certain sets of parameters.

In order to always satisfy the inequality (10), we propose to define the dimensionless relaxation moduli c_k^{ij} (indices ij will be omitted in the following) from a probability density function H of $log_{10}(\tau_k)$. Let us denote $x_k = log_{10}(\tau_k)$. As previously mentioned, all τ_k are evenly spaced with one value per decade, so the distance between two relaxation times in logarithmic scale is $\Delta = x_{k+1} - x_k = 1$. Our goal is to evaluate the c_k coefficient from H as follows :

$$c_k = \int_{x_k-\Delta/2}^{x_k+\Delta/2} H(x)\, dx \tag{11}$$

To the authors' point of view, this definition benefits from the property of a pdf. The associated cumulative density over the full range is one. To reproduce accurately the material response over a large range of time period, the number of relaxation times τ_k is large ($N = 14$ for Courtois et al. [11]). The number of relaxation times N has to be defined when identifying a material. In our approach, we choose to consider N such that $\sum c_k - 1$ is vanishingly small. With this definition, the evolution of $H(x)$ is fully connected to the stiffness evolution. When N is large enough, it is clear that $\sum c_k$ becomes close to 1 (as H is a pdf). Therefore, from equation (9), this leads to $\frac{C_\infty}{C_0} = 0$. In order to keep a non vanishing value of C_∞, we propose to replace H by qH in equation (11), with q a scalar between 0 and 1. At the limit (infinite number of τ_k), one gets a physical meaning of this additional parameter: $q = 1 - \frac{C_\infty}{C_0}$. In our work, the probability density function is built as the superposition of a normal distribution ($f(x)$, mean m, standard deviation s_1) and a skew normal distribution ($\phi(x)$, mean m, standard deviation s_2, shape parameter α), with w a parameter used to balance the relative weight of both functions:

$$H(x) = q(wf(x) + (1-w)\phi(x)), \tag{12}$$

with

$$f(x, m, s_1) = \frac{1}{s_1\sqrt{2\pi}} \mathrm{e}^{-\frac{1}{2}\left(\frac{x-m}{s_1}\right)^2}, \tag{13}$$

$$\phi(x, m, s_2, \alpha) = \frac{1}{s_2\sqrt{2\pi}} \mathrm{e}^{-\frac{1}{2}\left(\frac{x-m}{s_2}\right)^2} \left[1 + \mathrm{erf}\left(\alpha \frac{x-m}{s_2\sqrt{2}}\right)\right]. \tag{14}$$

The expression of c_k defined in equation (11) can be expressed in terms of cumulative density functions. Let $F(x, m, s_1)$ be the cumulative distribution function of the normal distribution and $\Phi(x, m, s_2, \alpha)$ the cumulative distribution function of the skew normal distribution. The dimensionless relaxation moduli $c_k = c(\tau_k)$ can thus be expressed as:

$$\begin{aligned} c_k = q\{&w[F(x_k + \Delta/2, m, s_1) - F(x_k - \Delta/2, m, s_1)] \\ &+ (1-w)[\Phi(x_k + \Delta/2, m, s_2, \alpha) \\ &- \Phi(x_k - \Delta/2, m, s_2, \alpha)]\} \end{aligned} \tag{15}$$

with

$$F(x, m, s_1) = \frac{1}{2}\left[1 + \mathrm{erf}\left(\frac{x-m}{s_1\sqrt{2}}\right)\right], \tag{16}$$

$$\Phi(x, m, s_2, \alpha) = F(x, m, s_2) - \frac{1}{\pi}\int_0^\alpha \frac{\mathrm{e}^{-\frac{1}{2}\left(\frac{x-m}{s_2}\right)^2 (1+x^2)}}{1+x^2}\, dx. \tag{17}$$

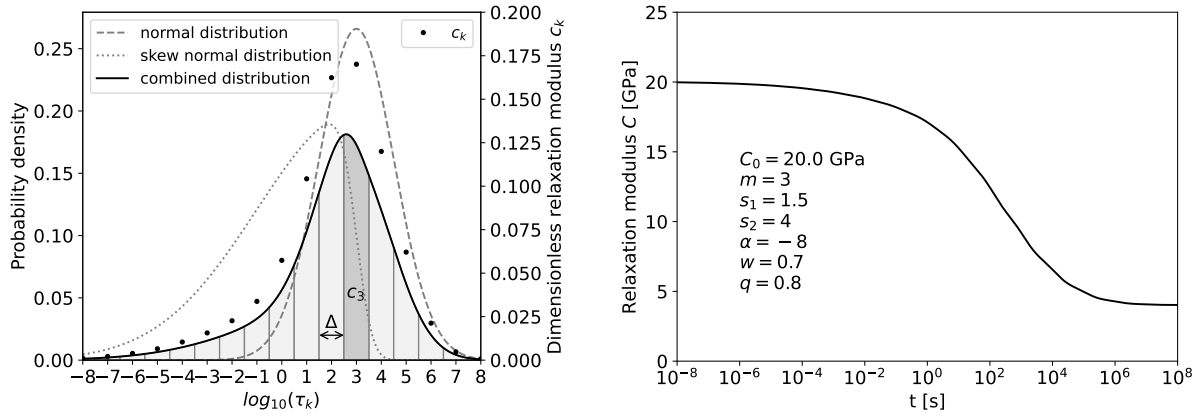

(a) (b)

Figure 4: (a) Schematic definition of the dimensionless relaxation moduli c_k. The probability density function H (equation (12)) is plotted in solid line. The c_k are computed as the integral between $x_k - \Delta/2$ and $x_k + \Delta/2$ (equation (11)). They are plotted as a function of $log_{10}(\tau_k)$ on the secondary axis of the graph. (b) For illustration, the relaxation function corresponding to the c_k is plotted as a function of time. The parameters used to describe the function are indicated on the figure and have been selected only for illustration of the model.

The logarithmic relaxation time x_k being fixed, only seven parameters are necessary for the definition of the family $(c_k)_{1\leq k\leq N}$. This strategy was already proposed by Courtois et al. [11] with a different definition. The key ingredient of our new proposition is the use of a pdf to determine c_k. So by construction, the condition (10) is always satisfied whatever the values of the seven parameters or the number of Prony coefficients and without additional normalization step.

With the proposed method, the pdf is fully responsible for the evolution of the relaxation function. In the present work, a combination of a normal and a skew normal was found to well describe the material behavior, but any pdf could be used to describe other materials with a different relaxation function.

Figure 4a illustrates graphically the computation of the c_k coefficients. The dashed line curve represents the normal distribution, the dotted line the skew normal distribution and the solid line the adopted probability density function H. For illustrative purpose, the following material parameters have been selected: $C_0 = 20\,\text{GPa}$, $m = 3$, $s_1 = 1.5$, $s_2 = 4$, $\alpha = -8$, $w = 0.7$ and $q = 0.8$. We propose in this example to define the material response on a time interval covering 17 decades. The coefficients c_k, evaluated based on equation (11), correspond to the area below the solid line curve, with a width of $\Delta = 1$, see Figure 4a. Figure 4b presents the evolution of one component of $\underline{\boldsymbol{C}}(t)$ defined by equation (3).

Note that a different relaxation function (and therefore a different spectrum equation) is necessary to describe each component of $\underline{\boldsymbol{C}}(t)$. In the case of an isotropic material with constant Poisson's ratio, only one relaxation function (and therefore one spectrum) has to be defined. For orthotropic materials, nine spectrum equations have to be determined.

3.3. Temperature effects

In Figure 3b, the shift factor $a_T = \frac{\tau(T)}{\tau(T_{ref})}$ has been experimentaly determined, assuming that the reference temperature is $T_{ref} = T_g$. The terms $\tau(T)$ and $\tau(T_{ref})$ are respectively the relaxation times at temperatures T and T_{ref}. In the literature, the evolution of a_T with temperature is described by various functions. An inflection point is usually observed at the glass transition temperature. Below the glass transition temperature T_g, an Arrhenius relationship is often adopted [11]. Above T_g, the WLF equation usually shows accurate agreement with experimental data [22]. a_T is sometimes described below T_g or over the full temperature range by a linear relationship or by an Arrhenius law with an activation energy varying with temperature [23, 24]. There is no definitive answer in the literature on a function that could suit all materials. Thorpe [25] studied the viscoelastic behavior of an epoxy resin on a temperature range including T_g. Three different functions were used to describe the shift factor evolution over the whole temperature range. Similar trends have been observed experimentally for the shift factor of the studied material. Above the glass transition temperature T_g, few experiments have been conducted in the present study, but an inflection point has been observed and the WLF equation will be used. Below T_g, exponential functions are adopted, such that the function is concave down, as observed experimentally. Finally, we propose the following description:

$$log(a_T) = \begin{cases} Q_1(1 - \mathrm{e}^{b_1(T-T_{ref})}) + Q_2(1 - \mathrm{e}^{b_2(T-T_{ref})}), & \text{if } T < T_{ref} \\ \dfrac{-D_1(T - T_{ref})}{D_2 + T - T_{ref}}, & \text{if } T_{ref} \leq T. \end{cases} \tag{18}$$

T_{ref}, Q_1, b_1, Q_2, b_2, D_1, D_2 are the parameters describing the shift function. T_{ref} is chosen here to be T_g. The function (18) has been fitted to the experimental results and is plotted on Figure 3b with a discontinuous black line. The identified parameters are: $Q_1 = 10.49$, $b_1 = 15.04 \times 10^{-3}\,\text{K}^{-1}$, $Q_2 = 0.7236$, $b_2 = 0.2250\,\text{K}^{-1}$, $D_1 = 9$, $D_2 = 52\,\text{K}$.

For time-dependent temperature loading, a reduced time t'

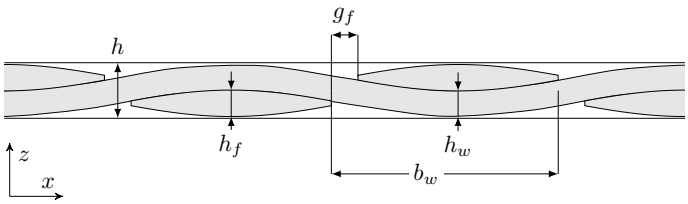

Figure 5: Layout of the weaving pattern of the studied composite. Some of the geometric parameters describing the weaving pattern are annotated.

is introduced to link time and temperature effects using a_T:

$$t' = \int_0^t \frac{ds}{a_T(T)} \tag{19}$$

When temperature remains constant, the reduced time becomes simply $t' = t/a_T$. The relaxation modulus at any time and temperature $E(t, T)$ can therefore easily be computed from the master curve $E(t', T_{ref})$.

3.4. Numerical implementation

As described by Zobeiry et al. [26], Crochon et al. [27], or Miana [28], two strategies have been adopted to implement viscoelastic models in finite element softwares. Recursive strategies have been widely used [26, 29, 30] and solved numerically the integral in equation (6). However, the convergence rate of these strategies is only of first order. Poon and Ahmad [31] have proposed to differentiate equation (6) and solved it using finite difference schemes. The advantage of such strategy is the existence in the literature of difference schemes with higher order convergence rates. Crochon et al. [27] proposed for example a fourth order Runge-Kutta scheme, applied to a Schapery-type constitutive theory.

By applying the method of Poon and Ahmad [31], the differentiated equation (6) becomes:

$$\frac{d\boldsymbol{q_k}}{dt} = \frac{d\boldsymbol{\varepsilon}}{dt} - \frac{1}{\tau_k}\boldsymbol{q_k} \tag{20}$$

This differential equation is solved based on the implicit Runge-Kutta Radau IIA scheme, with a stage value of $s = 3$ (fifth order accuracy). Finally, the material model presented above has been implemented in a user subroutine UMAT for use in the FE commercial code Abaqus. The main steps are presented in Appendix A.

4. Numerical model

The homogenization of the laminate is based on a two-scale model for the yarn and the woven composite. The geometric model and associated measurements are presented first. It relies mostly on SEM observations. Secondly, an inverse method based on FE calculations proposed by Girard et al. [7] is extended to capture the viscoelastic response of laminates.

4.1. Internal structure of the composite

In this section, the internal structure of the material is accurately defined by a combination of micro-tomography and SEM observations. The identified geometry is later represented in a 3D FE model to obtain the homogenized orthotropic behavior of the composite in the viscoelastic regime.

4.1.1. Geometric model

The considered material is composed of a glass fiber fabric and a thermoset resin. From micro-tomography and SEM observations, it is shown that the fabric is plain weave and only one layer of fabric is found in the thickness of the laminate of interest. While SEM images provide high magnification on cross-sections, the use of micro-tomography is helpful to ensure that a representative volume element (RVE) exists. In this work, x and y directions denote respectively the warp and fill directions of the composite, while z direction is the out-of-plane direction.

The present work extends the composite homogenization of Girard et al. [7] by modifying the geometric model. With the new proposition, a perfect fit between the crossing yarns along the whole surface of contact is ensured. Indeed, the fit was perfect only along the center line with the description provided in [7]. The main steps for building the RVE in ABAQUS are recalled next.

As proposed by Naik and Ganesh [32], the undulations of the yarns are described with a sinusoidal curve. From the micro-tomography scans, it has been checked that the crimp is identical in warp and fill directions on the studied composite, following indeed a sinusoidal curve. Figure 5 shows a layout of the considered composite, where an undulating warp yarn is represented along the x direction. The transverse (fill) yarns are observed in cross-section and their boundary coincide with the crossing warp yarn boundary. The fill yarns are separated by a distance g_f (respectively g_w for warp yarns). h_w and h_f are the thicknesses of the warp and fill yarns at their center. b_w and b_f describe respectively half an undulation period along the warp and fill directions.

Since the boundaries of crossing yarns coincide and the section of the yarns remains unchanged along their length (both assumptions were confirmed from SEM observations), a surface can describe the envelope of both warp and fill yarns. The surface undulates in the x direction with a period b_w and an amplitude $h_f/2$, and in the y direction with a period b_f and an amplitude $h_w/2$. Thus, the mathematical definition of the surface is:

$$z = \frac{h_w}{2} sin\left(\pi \frac{y}{b_f}\right) + \frac{h_f}{2} sin\left(\pi \frac{x}{b_w}\right) \tag{21}$$

This surface (plotted on Figure 6a) describes the bottom surface of one yarn as well as the top surface of one crossing yarn. By shifting this surface of half a period along x and/or y (i.e. by replacing x by $x + b_w$ and/or y by $y + b_f$), it is possible to describe all four needed surfaces to represent the top and bottom envelopes of all yarns. Figure 6b represents these four surfaces, and by drawing them only where necessary, one can

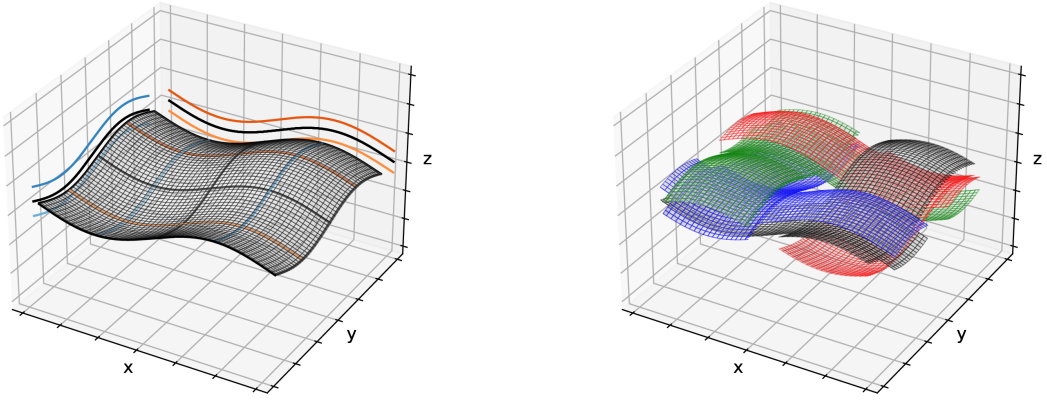

(a) (b)

Figure 6: (a) Surface described by equation (21). Particular contours are colored on the surface and projected on the walls of the graph ($x = \{-b_w, -b_w/2, 0, b_w/2, b_w\}$ and $y = \{-b_f, -b_f/2, 0, b_f/2, b_f\}$). Note that the projections of $x = \{-b_w, 0, b_w\}$ are coincident. A similar remark is observed on y projections. (b) Yarns described by the four necessary surfaces. The surface described by equation (21) is drawn in black. The surface shifted on x by an amount b_w is in red. The surface shifted on y by an amount b_f is in blue. The surface shifted on x by an amount b_w and on y by an amount b_f is in green. With further boolean operations, the plain weave pattern of the RVE is obtained.

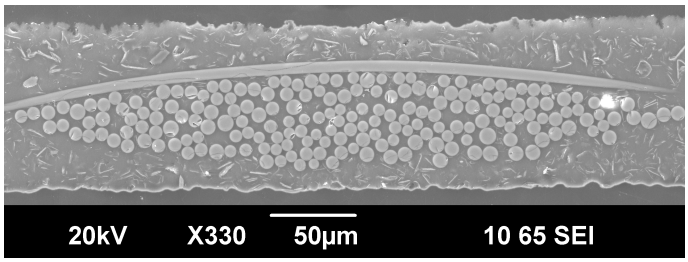

Figure 7: Scanning Electron Microscope (SEM) image of a warp yarn of the studied composite.

describe the four yarns composing a unit cell of the weaving pattern. With boolean operations in the FE software Abaqus, it is possible to represent the geometry of the complete composite with a perfect fit between crossing yarns and thus avoid small or distorted elements at crossing regions.

4.1.2. *Measurements of the geometric properties*

The shape of the RVE (depicted in Figure 5) is determined from micro-tomography. The average values of the geometrical dimensions, b_w and b_f are obtained by observing the cross-section of the composite under an optical microscope by considering ten consecutive unit cells. The values for h_w, h_f, g_w and g_f are obtained from SEM observations, following the method described in Girard et al. [7]. One image of a warp yarn is presented on Figure 7. One can notice that the inter yarns resin contains a small volume fraction of reinforcement (in comparison with Girard et al. [7]). Given the sparse distribution of fillers, we consider here that a single resin is present in the composite. More than 50 images have been taken in both warp and fill directions.

The average shapes of warp and fill yarns (black line on Figure 8) are determined by superimposition of all SEM observations. The geometric quantities characterizing the unit cell of the composite are summarized in Table 1. In addition, SEM observations on yarns provide the positions and diameters of all fibers for each yarn. The distribution of fiber diameters in the warp and fill directions is displayed in Figure 9a. From this information, the average volume fraction of fibers in each yarn are: 67.49 % and 67.79 % respectively (see Figure 9b).

From the shape of the yarns (Figure 8), the volume fractions of fibers (Figure 9b) and the overall geometric dimensions

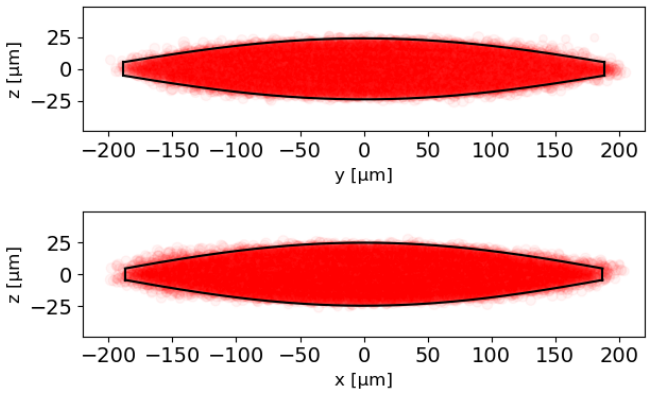

Figure 8: Superposition of all fibers detected on SEM observations for warp and fill yarns. 50 images are used for each direction. In total, more than 10 000 fibers are used to define the geometry of both yarns.

h	h_f	b_f	g_f	h_w	b_w	g_w
100.0	48.5	438.6	48.2	47.6	423.7	62.0

Table 1: Geometric dimensions describing the internal structure of the studied laminate (in μm). One may refer to Figure 5 for illustration.

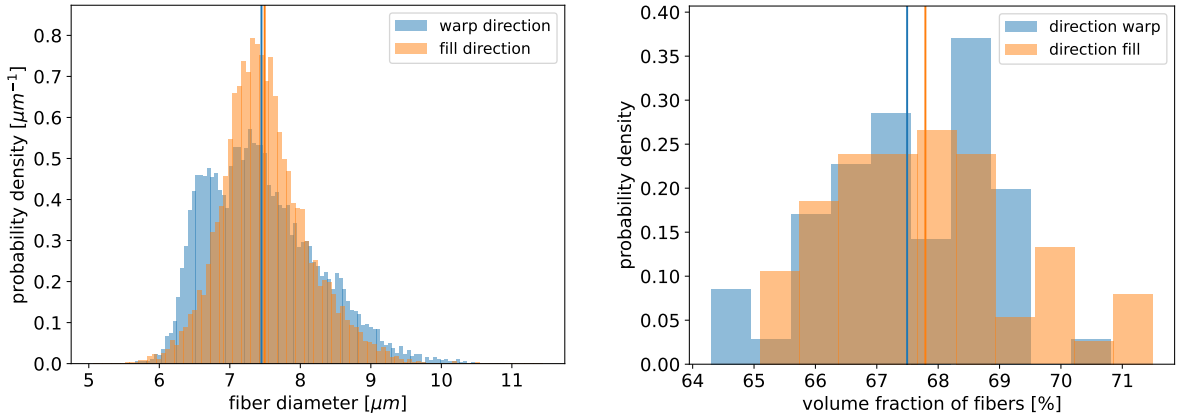

(a) (b)

Figure 9: (a) Distribution of the measured fiber diameters in warp and fill directions. The mean is very close, but the distribution is noticeably different for both directions. (b) Volume fraction of fibers in the yarns. For both plots, the vertical lines represent the mean in each direction.

(Table 1), it appears that the considered laminate is balanced. Microtomography results also showed that the crimp is similar in both directions. However, relaxation tests in $0°$ and $90°$ directions showed a substantial difference in the mechanical response. On Figure 9a, one can notice that the diameters of the fibers in the fill direction follow a unimodal distribution with a mean of $7.45\,\mu\text{m}$ and a standard deviation of $0.78\,\mu\text{m}$. Along the warp direction, the diameters of the fibers have a mean of $7.49\,\mu\text{m}$ and a standard deviation of $0.61\,\mu\text{m}$. Though the fibers along the warp or the fill directions have very similar means, diameters follow clearly a different distribution. It has been checked that the distribution does not vary from yarn to yarn, showing that the observed bimodal distribution in the warp direction is not the result of different unimodal distributions in separate yarns. The diameters of around $10\,000$ fibers compose each distribution. From the authors point of view, the difference in distribution may highlight the presence of two different kinds of glass fibers in the warp and the fill directions, explaining the different mechanical responses in both directions. In the following, D-glass and E-glass will be considered to compose respectively warp and fill yarns. This assumption will be qualitatively validated based on nanoindentation tests, later in Section 4.2.5.

4.2. *Two-scale homogenization method*

The visco-elastic orthotropic behavior of the woven composite is captured in two steps: (i) aligned glass fibers embedded into a resin are homogenized to get the behaviors of both yarns (ii) the RVE of the woven composite, containing yarns and resin is homogenized. The viscoelastic response obtained at the yarn scale feeds therefore the numerical model at the scale of the woven composite. In contrast to other works of the literature, [15] or [11], the resin response is initially unknown. An inverse method is thus proposed for identification of the viscoelastic response of the resin, which is assumed to be identical inside and around the yarns (see Figure 7). In Girard et al. [7], dedicated to hyperfrequency applications, the volume fraction of ceramic inclusions was large in the inter-yarn resin and two different materials had to be considered to model the inter- and the intra-yarn resins.

As in the works of Hirsekorn et al. [15], Courtois et al. [11] and Martynenko and Lvov [33], one relaxation time per decade will be adopted to describe the viscoelastic behaviors of the resin, of the yarns and of the woven composite. The temperature in simulations is considered uniform, constant in time, and corresponds to the reference temperature $T_{ref} = T_g$, adopted to construct the master curve. The simulations at the level of yarns or of the woven unit cell are run over the time range of the measurements for this reference temperature. Hirsekorn et al. [15] and Martynenko and Lvov [33] showed that the same shift function can be used for the resin and for the composite, so the shift function identified in Section 2.2 will be used to describe the time-temperature equivalence for the behaviors of the resin, the homogeneous yarns and the woven composite.

4.2.1. *Yarn homogenization*

Most studies consider a regular arrangement of the fibers in the yarn microstructure, see for instance Atintoh et al. [34]. As demonstrated in a previous work [7], this can lead to significant errors on estimated transverse moduli, especially for high volume fraction of fibers. In Girard et al. [7], for a volume fraction of $67\,\%$, the differences between a regular disposition of fibers and a random 3D RVE were as large as $10\,\%$ on E_T, $48\,\%$ on ν_T and $18\,\%$ on G_T.

Here, as in [7], random RVEs are considered. 100 random unit cells containing 10 fibers are generated (the radii of the fibers follow the experimental distribution presented in Figure 9a) and the elastic behavior of all cells is homogenized. Then the configuration which is the closest to the mean response of all unit cells is selected to model the viscoelastic yarn. Different RVEs are generated to model warp and fill yarns so as to account for the differences in volume fraction of fibers and radii distribution. Since we were not able to develop analytical models which could be as precise as FE simulations, we have

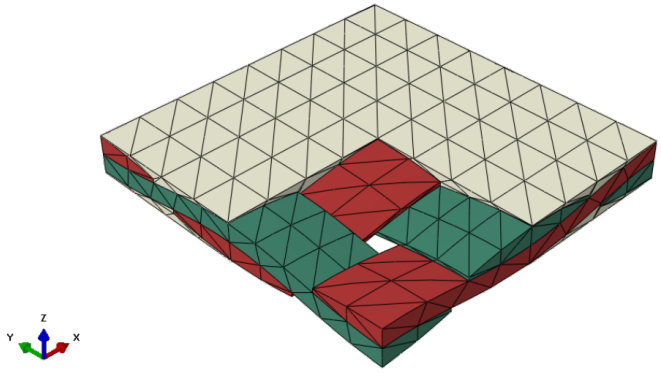

Figure 10: Numerical RVE of the studied woven composite. A quarter of the resin is hidden to present the fabric.

decided to keep this numerical step despite the higher numerical cost. More information about the duration of the simulation will be provided in the next section. No delamination effects between fibers are taken into account but the model could be adapted if necessary.

In the present work, 3D unit cells with one element in the fiber direction are tested. Periodic Boundary Conditions (PBCs) are applied so this configuration is representative of infinitely long fibers. More information on PBCs used in the finite element simulations can be found elsewhere, see for instance Appendix B of Girard et al. [7].

Six computations (1D strain loading case) are performed in order to obtain the mechanical behavior of the yarn. For each loading case, a constant strain tensor containing only one non-zero component is imposed to the yarn unit cell. In Voigt notation, with $i, j \in \{1, \dots, 6\}$, each loading case i (representative of unidirectional strain loading) is defined as: $\varepsilon_i = 0.005$ and $\varepsilon_j(t) = 0$ for all $j \neq i$. The volume average of the stress is computed in the whole model for each time step, allowing the computation of the components of $\underline{\boldsymbol{C}}(t)$: $C_{ij}(t) = \sigma_j(t)/\varepsilon_i$.

For all calculations performed at the level of the yarns, it has been checked that the relaxation tensor is representative of a transversely isotropic material (equation (2)), i.e. $C_{11} = C_{22}$, $C_{13} = C_{23}$, $C_{55} = C_{66}$ and $(C_{11} - C_{12})/2 = C_{66}$. Note that fibers are aligned along direction 3.

The numerical implementation of the viscoelastic constitutive law presented in section 3 requires a Prony series description of the relaxation tensor $\underline{\boldsymbol{C}}(t)$ (equation (3)). In our approach, the relaxation times are fixed to one per decade and therefore, the values for $\underline{\boldsymbol{C_\infty}}$ and $\underline{\boldsymbol{C_k}}$ have to be determined. A least squares regression is used to fit the spectra for each independent component $C_{ij}(t)$ describing the yarns behaviors. The homogenized behaviors of the yarns are later used for the homogenization at the level of the woven composite.

4.2.2. *Woven composite homogenization*

Similarly to the previous section on yarn homogenization, PBCs are also applied to the unit cell of the woven composite. The same procedure as for the yarns can be applied to assess the relaxation tensor $\underline{\boldsymbol{C}}(t)$ by applying six elementary 1D strain loadings. It has been checked that the material exhibits an orthotropic behavior: the relaxation tensor is symmetric and has the shape presented in equation (2).

The geometry of the woven composite is shown on Figure 10. A mesh convergence study has been run by homogenizing the elastic behavior of the composite. The homogeneous properties are little sensitive to the mesh: a difference smaller than $0.2\,\%$ on the estimated elastic moduli between models containing 4000 and $100\,000$ nodes was observed. The mesh with 4000 nodes presented in Figure 10 is therefore adopted for the following simulations, allowing faster computation times, which make it convenient for the inverse method.

Note that in this phase of modeling, the yarns are considered as homogeneous materials. This approximation is justified in the present case, with 200 fibers composing each yarn and for small strains, where localization effects are limited. However, this assumption may not be so well suited for different glass fabrics containing only tens of fibers or very spread yarns with only one or two fibers in the thickness direction.

4.2.3. *Inverse method for identifying the behavior of the resin*

At this stage the response of the resin is still unknown, so the viscoelastic behaviors of the yarns and of the composite can not be obtained. To identify the resin response, an inverse method is proposed, based on the experimental viscoelastic response of the composite captured in uniaxial tension for the three orientations tested ($0°$, $45°$ and $90°$). In this case, only one component of the strain tensor has to be imposed in the loading direction while the other components are adjusted by the FE software so as to obtain overall free surfaces in the transverse directions.

In the present study, the PBCs are managed using reference points accounting for displacements between two opposite faces in the reference coordinate system. Applying a uniaxial tension in one direction of this coordinate system is easily done, as explained in Appendix B of [7]. On the contrary, applying a uniaxial tension in an arbitrary direction is not straightforward. This is however necessary to compare numerical results to experiments carried out for the $45°$ direction. A new method to achieve this goal is presented next. The idea is to apply the PBCs in the original coordinate system using three reference points. Three additional reference points are responsible for the description of the loading in a transformed frame. A set of equations links the displacements of the three first reference points to the three others. This set of equations is responsible for the change of frame. By using this method, a uniaxial loading can be applied in the transformed coordinate system, for any rotation with respect to the original frame (where the PBCs are defined). More details are given in Appendix B.

The three orientations tested experimentally ($0°$, $45°$ and $90°$) can therefore be modeled. Experimental and numerical results can be compared. Note that our method is general and can be adopted for any arbitrary angle.

As explained in section 4.1.2, from the balanced geometry of the composite (similar crimp, shape of yarns, volume fraction of fibers), the difference in measured Young's moduli in

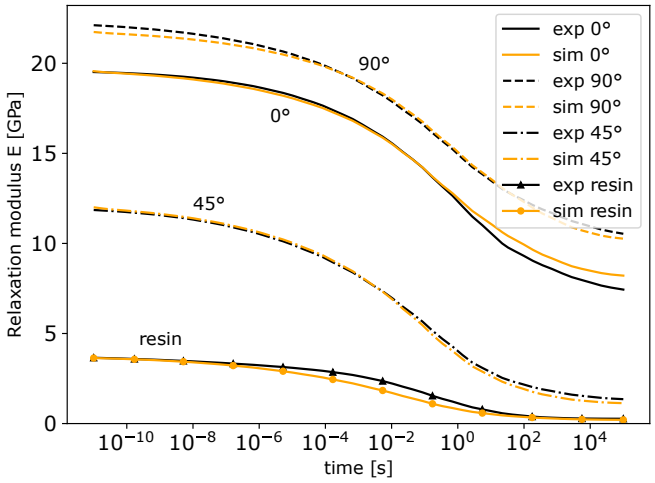

Figure 11: Time evolution of the relaxation modulus. The experimental and numerical responses of the composite under uniaxial tension in directions 0°, 45° and 90° are compared. The response of the identified resin is also compared to the experimental measurements. More details on the resin will be provided in section 4.2.5.

the 0° and the 90° directions can only be explained by different elastic properties for the glass fibers in both directions. From this observation, it has been deduced that the glass fibers in both directions must have different elastic properties. The different distributions of fibers radii may support this assumption. In the PCB industry, E-glass is the most commonly employed, and its elastic behavior is usually described by $E_f = 72.3\,\text{GPa}$, $\nu_f = 0.22$ [6]. D-glass is also used for its superior dielectric constant, and presents a smaller Young's modulus of 51.7 GPa, as presented by Li and Watson [35]. We assume that this difference in glass Young's moduli could explain the differences observed experimentally. The behavior of the glass fibers is thus supposed to be known, linear elastic, temperature- and time-independent, with D-glass in the warp (0°) direction and E-glass in the fill (90°) direction.

For the studied composite, the same resin is assumed to be present inside and between yarns. The unknown behavior of the resin is expected to be isotropic linear viscoelastic, with a constant Poisson's ratio, as it is often the case in the literature [9, 10, 33, 36]. Assuming a constant Poisson's ratio for the resin will not lead to a constant Poisson's ratio for the composite, see later in Figure 14b. Note that some authors make the hypothesis of a constant bulk modulus [37]. Therefore, only one time-dependent relaxation modulus has to be determined for the resin. The optimization method described below is used to identify the parameters of the continuous function (15) describing the relaxation moduli:

1. estimation of the parameters describing the resin viscoelastic behavior
2. homogenization of the yarns (warp and fill)
3. numerical tensions at the woven level in 0°, 45° and 90° orientations
4. comparison between experimental and numerical results and new estimate for the resin parameters (back to step 1.)

E_0 [GPa]	ν	m	s_1	s_2	α	w	q
3.740	0.466	-1.447×10^{-4}	2.141	5.152	−6.386	0.304	0.947

Table 2: Parameters describing the mechanical response of the resin, obtained from the optimization procedure at the composite level. The characteristic times are chosen as one per decade, ranging from 1×10^{-16} s to 1×10^{6} s.

The comparison between experimental and numerical results is done through an error function:

$$f_{cost} = \left\langle \left(\frac{E^{exp}_{0^\circ}(t) - E^{sim}_{0^\circ}(t)}{E^{exp}_{0^\circ}(t=0)} \right)^2 \right\rangle + \left\langle \left(\frac{E^{exp}_{45^\circ}(t) - E^{sim}_{45^\circ}(t)}{E^{exp}_{45^\circ}(t=0)} \right)^2 \right\rangle + \left\langle \left(\frac{E^{exp}_{90^\circ}(t) - E^{sim}_{90^\circ}(t)}{E^{exp}_{90^\circ}(t=0)} \right)^2 \right\rangle \tag{22}$$

where the angle brackets indicate the arithmetic mean over the time interval. The subscripts refer to the orientation of the test and the superscripts to the experimental or simulated nature of the relaxation modulus. The Nelder-Mead optimization algorithm is used to minimize the error function by finding the optimal set of parameters for the resin behavior. The function presented in section 3.2 to describe the relaxation moduli allows a full definition of the viscoelastic behavior of the resin over more than 13 decades of time assessed experimentally see Figure 3a with only eight parameters: E_0, ν, m, s_1, s_2, a, w, q. This model formulation is thus well suited for such an optimization problem. For the considered material, the number of terms in the Prony series is chosen to be $N = 23$. It has been checked that for larger values of N, E_∞ is not affected, meaning that additional relaxation time will be weighted by negligible dimensionless relaxation moduli $c_k \approx 0$.

4.2.4. *Homogenization results*

Initial values for $E_0 = 3.05\,\text{GPa}$ and $\nu = 0.33$ are taken from the work of Chen et al. [6]. The initial values for m, s_1, s_2, a, w, q are chosen arbitrarily. One homogenization at the mesoscale over the whole relaxation spectrum takes about 14 min on a 24 cores computer. Less than 200 iterations were necessary to minimize the cost function and identify the resin, yarns and woven viscoelastic behaviors on the whole range of time and temperature. This corresponds to approximately 2 days of computation. After the optimization procedure, the numerical results best fitting the experimental measurements (Figure 11) and the estimated viscoelastic parameters of the resin are obtained (presented in Table 2). Note that the results are insensitive to the initial set of parameters. A very good agreement is observed between the experimental responses in the three considered orientations and the corresponding numerical estimates. One can therefore be confident in the mechanical behavior identified for the resin. Such a good fit could not be obtained using

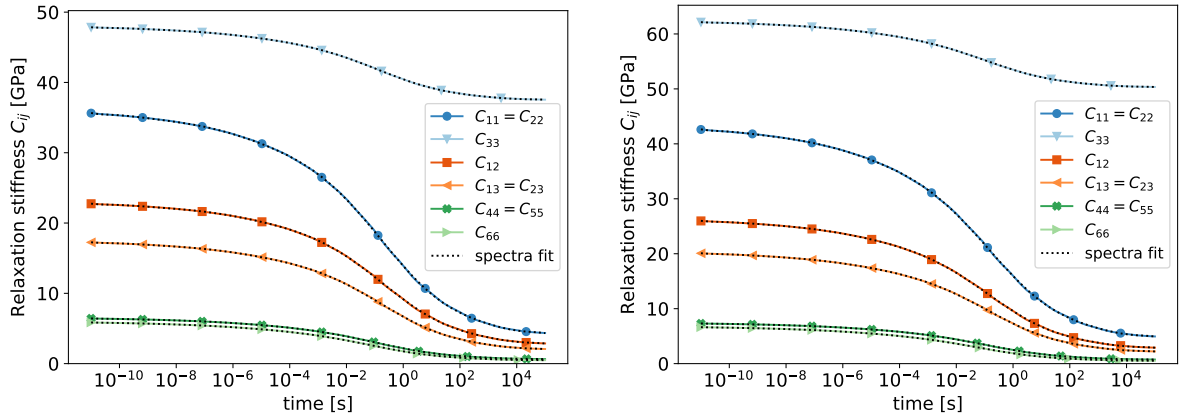

(a) (b)

Figure 12: Evolution with time of the non-zero components of the relaxation stiffness tensor obtained by homogenization for (a) warp and (b) fill yarns, at the reference temperature T_g. The viscoelastic behavior of the resin is described by the parameters in Table 2.

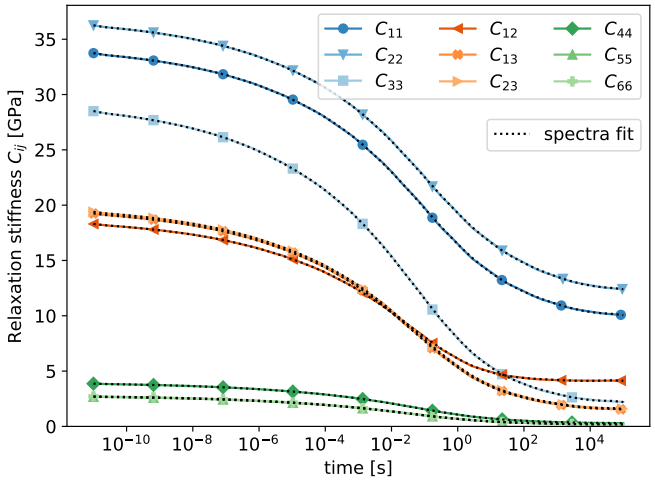

Figure 13: Evolution with time of the non-zero components of the relaxation stiffness tensor obtained by the two-scale FE homogenization for the considered composite, at the reference temperature T_g.

	C^0_{ij} [GPa]	m	s_1	s_2	α	w	q
$C_{11}(t)$	35.94	0.3371	1.985	4.952	-13.26	0.5381	0.8826
$C_{33}(t)$	47.96	0.2815	2.003	5.004	-11.33	0.5011	0.2180
$C_{12}(t)$	22.91	0.3356	1.964	4.890	-17.69	0.5647	0.8780
$C_{13}(t)$	17.40	0.3217	1.979	4.937	-13.93	0.5391	0.8841
$C_{44}(t)$	6.498	0.2272	2.004	5.000	-10.47	0.4778	0.9041

Table 3: Parameters describing the transversely isotropic viscoelastic response of the warp yarn, obtained by homogenization with the behavior of the resin described in Table 2. The characteristic times are chosen as one per decade, ranging from 10^{-16} s to 10^{6} s.

	C^0_{ij} [GPa]	m	s_1	s_2	α	w	q
$C_{11}(t)$	43.01	0.3071	1.998	4.969	-11.91	0.5168	0.8888
$C_{33}(t)$	62.29	0.2350	2.013	5.012	-10.44	0.4792	0.1924
$C_{12}(t)$	26.21	0.2706	1.981	4.922	-13.46	0.5203	0.8922
$C_{13}(t)$	20.27	0.2745	1.994	4.956	-11.98	0.5081	0.8938
$C_{44}(t)$	7.393	0.2460	2.021	5.031	-10.01	0.4729	0.9028

Table 4: Parameters describing the transversely isotropic viscoelastic response of the fill yarn, obtained by homogenization with the behavior of the resin described in Table 2. The characteristic times are chosen as one per decade, ranging from 10^{-16} s to 10^{6} s.

the same E-glass behavior for fibers in both directions. In that case, the responses in 0° and 90° directions were almost identical (20.5 MPa and 20.8 MPa respectively for the instantaneous modulus).

Once the viscoelastic parameters of the resin have been assessed through the inverse method, based on the two-scale homogenization procedure, it is interesting to note that the homogenized behaviors of the yarns are a direct outcome (Figure 12, spectra parameters in Tables 3 and 4). At the woven composite level, the time evolution of the nine independent components of the stiffness matrix C_{ij} are plotted on Figure 13. The corresponding parameters for the spectra are determined to model each $C_{ij}(t)$ describing the orthotropic viscoelastic behavior of the material (see Table 5).

From the relaxation stiffness tensor components C_{ij}, it is possible to compute tensile and shear relaxation moduli (Figure 14a) as well as Poisson's ratios at the level of the composite (Figure 14b). Note that E_1 and E_2 moduli correspond to directions 0° and 90° and are already presented on Figure 11. One can notice that though the Poisson's ratios of the resin and of the glass fibers are assumed constant, it is not the case at the composite level. The two Poisson's ratios ν_{13} and ν_{23} have very similar values, as the shear moduli G_{13} and G_{23}.

As detailed by Tschoegl et al. [38], it is necessary to measure the time-dependency of the Poisson's ratio to perfectly assess the viscoelastic behavior of an isotropic material, such as the resin in the present study. However, its measurement over a long period of time is very complicated and often inaccurate. Due to the small strain amplitudes applied and the contactless strain measurement method, the signal to noise ra-

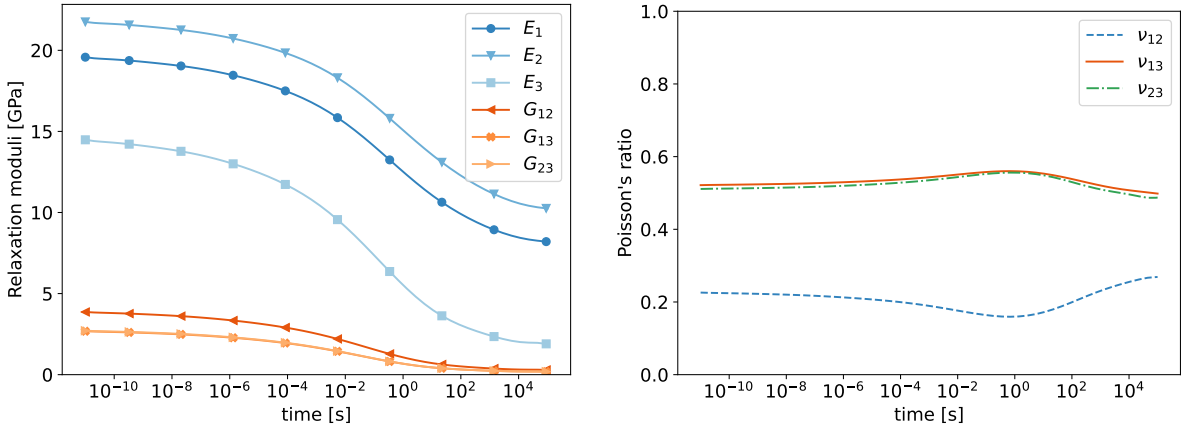

(a) (b)

Figure 14: Time evolution of (a) relaxation moduli and (b) Poisson's ratios obtained from the homogenization of the considered composite at the reference temperature. E_1 and E_2 correspond to the relaxation moduli for directions $0°$ and $90°$, already displayed in Figure 11.

	C^0_{ij} [GPa]	m	s_1	s_2	α	w	q
$C_{11}(t)$	34.16	0.2632	2.241	5.342	−8.183	0.4815	0.7117
$C_{22}(t)$	36.70	0.3225	2.312	5.451	−7.943	0.5082	0.6700
$C_{33}(t)$	28.93	0.07679	2.040	5.080	−8.456	0.4076	0.9266
$C_{12}(t)$	18.52	−0.5351	1.492	4.751	−4.579	0.3800	0.7772
$C_{13}(t)$	19.54	0.05970	2.034	5.066	−8.358	0.4010	0.9242
$C_{23}(t)$	19.68	0.06966	2.041	5.069	−8.525	0.4052	0.9221
$C_{44}(t)$	3.919	0.05433	2.029	5.111	−8.754	0.4104	0.9279
$C_{55}(t)$	2.728	0.02361	2.086	5.163	−7.332	0.3626	0.9361
$C_{66}(t)$	2.760	0.02124	2.084	5.159	−7.345	0.3619	0.9365

Table 5: Parameters describing the orthotropic viscoelastic response of the woven composite, obtained from the FE homogenization of the composite with the resin and both fill and warp yarns (parameters of Tables 2, 3 and 4). The characteristic times are chosen as one per decade, ranging from 10^{-16} s to 10^{6} s.

tio on the transverse strain was too small to be properly analyzed. Neither the Poisson's ratio of the resin, nor the one of the woven composite could be obtained and compared to the numerical predictions. The so-obtained constitutive behaviors for the resin and the composite material can therefore be employed with confidence for structural applications. In Section 5, a classic example for PCB is depicted.

4.2.5. Validation of the inverse method

Pure resin samples could not be obtained from the manufacturer. Thus, the following strategy is adopted to get samples of pure resin from pre-impregnated materials. First, cavities are cut in B-stage laminates, slightly larger than a tensile test sample (length 90 mm and width 20 mm). The pre-impregnated layers are later subjected to the lamination process recommended by the manufacturer, using the LPKF MultiPress S machine available at UFR MIM, Université de Lorraine. During this process, the resin contained in the B-stage laminates flows and fills the cavity. The cavity has to be cut with care to avoid any glass fibers to flow with the resin. At the end of the lamination process, the resin is cured. A tensile test sample of same size as those presented on Figure 1 (length 84 mm, width 15 mm, thickness 300 µm) is finally cut from the laminate sheet. Relaxation tests are performed on these samples, following the procedure defined in section 2. The master curve identified from these tests is presented on Figure 11 in comparison with the numerically identified resin response (outcome of the inverse method). A close match is found between those curves. From the experimental measurements on the resin, the assumption of identical shift function between the resin and the woven composite is validated.

In the homogenization procedure, it is assumed that D- and E-glass fibers compose yarns in warp and fill directions. To confirm the observation of Figure 9a showing different distributions, which could be a signature of different kinds of fibers, nanoindentation experiments have been performed in LEM3. With a Berkovich tip nanoindentor (CSM NHT^2) and using the Oliver and Pharr [39] method with a Poisson's ratio of 0.22, Young's modulus is measured on three fibers in each direction. The results show a Young's modulus of (66 ± 2) GPa in the warp direction and (77 ± 2) GPa in the fill direction. Although the values found in the literature for D-glass and E-glass could not be retrieved, a significant difference has been identified for fibers along the warp and fill directions. This additional experiment justifies the choice for different glass types in each direction.

These tests made on fibers and on pure resin validate the method presented in this work. The pure resin is seldomly available for mechanical testing. Manufacturers do not provide precise information because of confidentiality. In most cases, it is not possible to extract it from the laminate because it does not flow like the present resin. For other laminates, the intra-yarn resin is highly different from the inter-yarn resin (with a large volume content of inclusions, see [7]). In that case it would not be possible to extract both resins separately or even any resin at all, since a large amount of filler can prevent the resin to flow properly. The inverse method presented here is applicable in any case and has been validated with the particular composite studied. The method relies only on conventional tensile tests at $0°$, $45°$ and $90°$ on the composite material and FE compari-

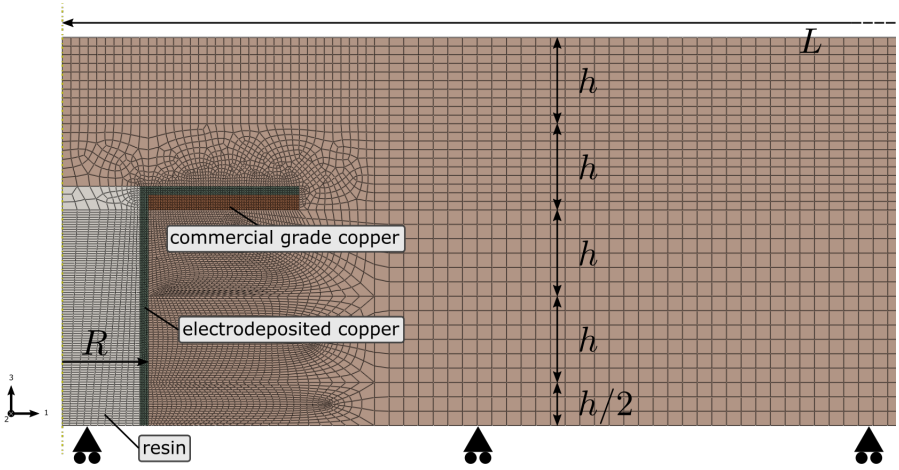

Figure 15: Model of the buried hole and FE mesh. The axis of symmetry is on the left of the figure. The far right side of the model is not presented. The model has a length of $L = 2\,\mathrm{mm}$ and a total thickness of $900\,\mu\mathrm{m}$.

son on RVEs subjected to specific PBCs (proposed in Appendix B). It allows at the same time the evaluation of the constitutive behavior of the resin, the yarns and the woven composite.

5. Application: Role of viscoelasticity in lifetime prediction of printed circuit board

As an application of the identified viscoelastic behaviors, we considered a buried hole in a PCB subjected to different thermal loads. The effects of the heating rate and of the temperature range on the plasticity development in copper are analyzed using FE simulations.

5.1. FE model

A buried hole in a ten layer PCB is considered, where the hole is filled by the resin of the pre-impregnated material. In the industry, the copper layers are numbered from one side of the PCB to the other. In the present study, the buried via connects layer 3 to layer 8. The geometry of the FE model is presented on Figure 15. The model is axisymmetric and represents a small portion of a real ten layer PCB. The considered PCB has a symmetric stack-up so only half of the thickness is modeled.

The mechanical behaviors of insulating layers and resin have been identified in previous sections. Copper parts are modeled with an elastic-plastic constitutive law, with combined isotropic and kinematic hardening, identified using the method presented in [40]. The thickness of copper is $17.5\,\mu\mathrm{m}$ for the commercial grade and $10\,\mu\mathrm{m}$ for the electrodeposited grade. The copper behavior is considered here as independent of time and temperature in order to focus on the sole effect of the viscoelastic behavior of the laminate and the resin. For comparison purpose, a similar analysis where the insulating laminate and the resin have a thermo-elastic behavior will be carried out.

The coefficients of thermal expansion (CTE) of all materials have been measured with the Netzsch TMA 402 Hyperion F3 equipment available at LEM3. The materials were tested in the range $[-70\,^\circ\mathrm{C}\ ;\ 200\,^\circ\mathrm{C}]$ with three successive heat ramps at $4\,\mathrm{K\,min^{-1}}$. The CTE of copper was observed to be constant over the temperature range of interest, with a value of $17.6 \times 10^{-6}\,\mathrm{K^{-1}}$. The CTE of the resin is consistent with the behavior of an epoxy, with a value around $50 \times 10^{-6}\,\mathrm{K^{-1}}$ below T_g and $120 \times 10^{-6}\,\mathrm{K^{-1}}$ over T_g. For the laminate, the measured in-plane expansion was observed to be almost constant with a value around $13.5 \times 10^{-6}\,\mathrm{K^{-1}}$ in $0°$ direction and $12.5 \times 10^{-6}\,\mathrm{K^{-1}}$ in $90°$ direction. The out-of-plane expansion was measured in the range 40 to $60 \times 10^{-6}\,\mathrm{K^{-1}}$ below T_g and $270 \times 10^{-6}\,\mathrm{K^{-1}}$ over T_g. These values are consistent with the datasheet of the supplier. The measured curves (CTEs as a function of temperature) are used in the simulation for resin and laminate.

The PCB is initially at room temperature (here $20\,^\circ\mathrm{C}$), assumed stress-free. During heating in a climate chamber, heterogeneity of the temperature field may exist in the PCB. The characteristic time for heat diffusion $\mathcal{T}$ is L_c^2/D, with L_c the characteristic length and $D = \lambda/\rho c$ the diffusivity. λ denotes the thermal conductivity, ρ the density and c the specific heat capacity. Considering that the PCB is mostly made of insulating laminates, a value of $\mathcal{T} = 1.3\,\mathrm{s}$ is obtained. One can thus conclude that for thermal loads applied in more than a few seconds, the uniformity of the temperature is verified. Therefore, in the present analysis, it is assumed that the temperature remains uniform during all cycles.

In the present work, the temperature amplitude $[-50\,^\circ\mathrm{C}\ ;\ 150\,^\circ\mathrm{C}]$ is adopted as a reference. This test condition is often required in automotive PCB standards. Note that thermal cycles with an amplitude of $200\,^\circ\mathrm{C}$ are also often encountered in standards for space applications. Three different thermal cycles have been simulated for comparison:

- $1\,\mathrm{K\,min^{-1}}$ heating and cooling rates, with $400\,\mathrm{min}$ hold times, $t_{cycle} = 72\,000\,\mathrm{s}$,
- $20\,\mathrm{K\,min^{-1}}$ heating and cooling rates, with $20\,\mathrm{min}$ hold times, $t_{cycle} = 3600\,\mathrm{s}$,
- $400\,\mathrm{K\,min^{-1}}$ heating and cooling rates, with $1\,\mathrm{min}$ hold

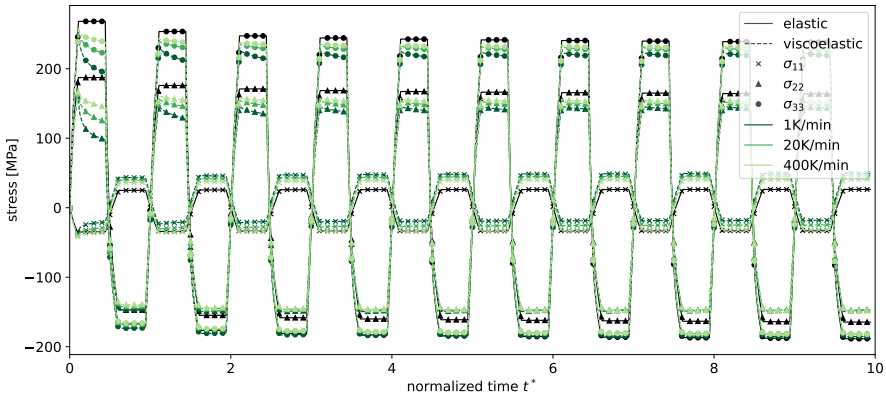

Figure 16: Evolution of stress components in the center of the copper via (at the plane of symmetry) over normalized time for ten thermal cycles $[-50\,^\circ\mathrm{C}\,;\,150\,^\circ\mathrm{C}]$. The stress component σ_{12} is not presented on the figure, its value being always negligible.

times, $t_{cycle} = 180\,\mathrm{s}$.

Note that the hold times are identical for the low and high temperature plateaus. All phases of the 3 cycles are proportional. For comparison of results on the same graph, the normalized time t^* is introduced: $t^* = t/t_{cycle}$ (see Figure 16).

Next, relaxation effects are also investigated by varying the heating rate while keeping the cycle duration constant, resulting in different hold times. The effect of the maximum temperature in the cycle is also assessed by applying different conditions: $[-50\,^\circ\mathrm{C};\ 150\,^\circ\mathrm{C}]$, $[-30\,^\circ\mathrm{C};\ 170\,^\circ\mathrm{C}]$ and $[-10\,^\circ\mathrm{C};\ 190\,^\circ\mathrm{C}]$, always keeping the same temperature amplitude $\Delta T = T_{max} - T_{min} = 200\,^\circ\mathrm{C}$. For comparison, simulations have also been performed by modeling the insulating laminates and resin with a thermo-elastic constitutive behavior. The thermo-elastic behaviors have been obtained from the viscoelastic one by fixing a response time of $1\,\mathrm{s}$.

5.2. *Stress relaxation and plasticity development in a buried via*

The buried via is subjected to ten thermal cycles $[-50\,^\circ\mathrm{C}\,;\,150\,^\circ\mathrm{C}]$. The resulting stresses in the center of the copper via, at the plane of symmetry, are presented on Figure 16, where the structure is expected to fail due to low-cycle fatigue (as observed in experiments on PCBs). On the figure and in the following, σ_{11} designates the radial stress, σ_{22} the hoop stress and σ_{33} the axial stress. The evolution of stresses is described in the following paragraph for each phase of the temperature cycle.

(i) In the first stage of the simulation, the temperature increases from $20\,^\circ\mathrm{C}$ to $150\,^\circ\mathrm{C}$ and the value of σ_{33} rises because of the difference of the coefficients of thermal expansion (CTE) between copper, resin and laminates. The induced strain ε_{33} in the copper via, combined with plastic incompressibility, lead to a significant rise of σ_{22}, which could not be explained by CTE mismatch alone. In the 1 (radial) direction, the CTE of the resin filling the hole is larger than the one of the copper via or of the surrounding composite laminates. Therefore when the temperature rises, compressive σ_{11} stresses develop in the resin and in the copper via, which is sealed between resin and laminates. Stress values at the end of the heating phase are little affected by the heating rate. (ii) During the second phase, the temperature is held constant at T_{max} for a different time duration depending on the load case. Stresses relax in the case of viscoelastic materials, and this effect is more pronounced when the hold time is larger. (iii) The cooling phase is very similar for all presented cases. Stresses σ_{22} and σ_{33} decrease and reach negative values. This is again explained by the mismatch in CTE and plastic incompressibility. σ_{11} rises and reaches positive values, for the same reason as during the first ramp (larger CTE of the resin). (iv) In the last phase of the cycle, the temperature is held constant at T_{min}. No noticeable relaxation is observed in this phase, since materials are in the glassy state. Accommodation is observed after a few cycles, mainly due to the kinematic hardening of copper.

When the resin filling the via and the insulating laminates are described by a thermo-elastic constitutive behavior, results are independent of the heating and cooling rates or of the hold times. This is expected since in this case, all employed constitutive behaviors are independent of time. Note that the maximum stress for all conditions reach almost the same value.

The accumulated plastic strain p along ten cycles is shown on Figure 17 for the point located at the plane of symmetry. It presents a regularly increasing curve. It is observed that the higher the heating rate is, the closer the response is to the elastic case. Nevertheless, the value of p after 10 cycles is relatively close for all three heating rates, and is also very close to the elastic case. This can be explained by results on Figure 16. Since the maximum stresses are similar for all conditions, the plastic strain develops the same way and is not affected by the later occurring relaxation. The fatigue response of the considered copper grade has also been studied in Girard et al. [40]. The Coffin-Manson relation has been identified to relate the accumulated plastic strain increment Δp to the number of cycles to failure N_f. From the accumulated plastic strain increment Δp computed for each configuration, a corresponding number of cycles to failure could be estimated:

- $N_f = 4948$ cycles for the viscoelastic case with a

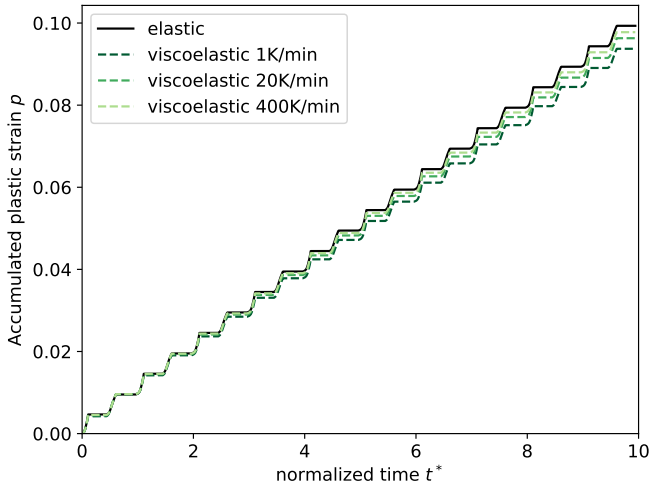

Figure 17: Accumulated plastic strain over normalized time in the center of the copper via for ten thermal cycles [$-50\,^\circ$C ; $150\,^\circ$C] and different durations of the temperature cycle.

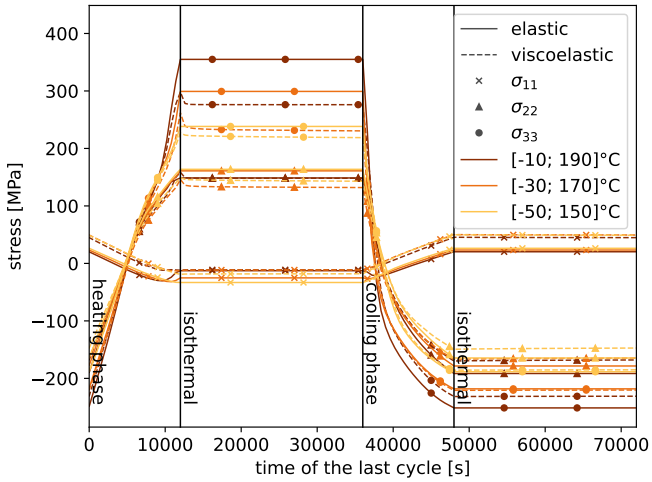

Figure 18: Evolution of stress components in the center of the copper via (at the plane of symmetry) over time for the tenth thermal cycle. Three different temperature ranges are considered with identical $\Delta T = 200\,^\circ$C. The heating and cooling rate is $1\,\mathrm{K\,min^{-1}}$ and the hold time is $400\,\mathrm{min}$. The stress σ_{12} is not presented on the figure, its value being always negligible.

$1\,\mathrm{K\,min^{-1}}$ heating rate,

- N_f = 4686 cycles for the viscoelastic case with a $20\,\mathrm{K\,min^{-1}}$ heating rate,
- N_f = 4542 cycles for the viscoelastic case with a $400\,\mathrm{K\,min^{-1}}$ heating rate,
- N_f = 4388 cycles for the elastic case.

Next, the effect of the maximum temperature is investigated, keeping similar heating rate ($1\,\mathrm{K\,min^{-1}}$), hold time ($400\,\mathrm{min}$) and temperature amplitude ($200\,^\circ$C). Stress evolution in the center of the copper via are presented on Figure 18 for the tenth thermal cycle. It can be observed that a larger maximum temperature leads to higher σ_{33} stress (for both elastic or viscoelastic cases, even for identical ΔT). In the out-of-plane direction (3), the CTEs of the resin and laminates are significantly larger than the CTE of copper. In addition, the CTEs of resin and laminate rise with temperature. Close to T_g, the increase of CTE is accompanied with a reduction of the stiffness. However, as seen on Figure 18, these two counteracting effects do not compensate and σ_{33} always rises with temperature. For temperature close to or above T_g, the stress difference between the elastic and the viscoelastic predictions becomes important. This difference does not only come from the relaxation during the hold time at large temperature. Indeed, it already exists during the heating phase. Therefore when a PCB encounters temperature excursions close to or over T_g, adopting an elastic description for the constituents is too conservative and is not adequate for lifetime predictions. Large differences in the accumulated plastic strain are observed in Figure 19, especially when $T_{max} = 190\,^\circ$C. The estimated number of cycles to failure is presented in Table 6 for the six different cases. Note that in our approach, the copper behavior is temperature and rate independent. It is expected that the yield stress of copper will

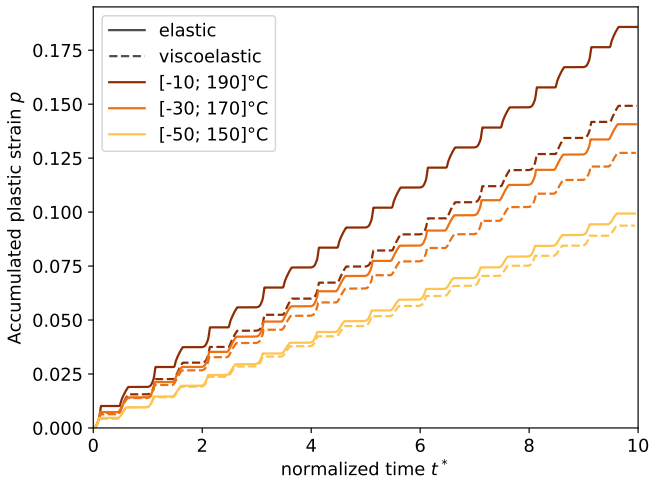

Figure 19: Accumulated plastic strain over normalized time in the center of the copper via for ten thermal cycles and three temperature ranges. The cycle duration and the temperature amplitude ΔT are the same for all cases.

decrease at larger temperature. So the difference in accumulated plastic strain (and also lifetime) between scenarios could be even larger.

6. Conclusion

A coupled experimental and numerical approach is presented to analyze the viscoelastic behavior of a woven composite used in Printed Circuit Boards. Experimental observations have been made on the composite in order to precisely describe its microstructure needed for the numerical model. Experimental tensile relaxation tests have been performed on the material at dif-

constitutive behavior	$[-50\,°C\,;\,150\,°C]$	$[-30\,°C\,;\,170\,°C]$	$[-10\,°C\,;\,190\,°C]$
elastic	4388	2433	1502
viscoelastic	4948	2954	2207

Table 6: Estimated number of cycles to failure for the buried via subjected to different temperature ranges. The heating rate is set to $1\,\mathrm{K\,min^{-1}}$. The hold time is $400\,\mathrm{min}$ and the temperature amplitude $200\,°C$. The predictions based on elastic and viscoelastic constitutive behaviors are compared.

ferent temperatures to characterize its viscoelastic response. A new experimental setup has been proposed to avoid oxidation effects at high temperature, while still being able to perform DIC strain measurements. Strain measurements in the plane of the woven composite are captured during tensile tests at $0°$, $45°$ and $90°$. Based on experiments, relaxation master curves using the time-temperature superposition principle are obtained. However, the noise in transverse strain measurements prevent the assessment of the Poisson's ratio. This point concerning the difficulty to measure Poisson's ratio with time has been noticed by Tscheogl [38] and constitutes a prospect for the present study.

The constitutive material model employed to describe the behavior of the composite is the generalized Maxwell model. The model has been implemented in Abaqus with a UMAT subroutine. A Runge-Kutta integration scheme is exposed in Appendix A. A new spectrum equation is proposed to limit the number of coefficients describing the viscoelastic behavior of the resin. This new spectrum equation ensures by construction that the sum of all dimensionless Prony coefficients c_k is smaller than one (equation (10)), making the new proposition better suited to the inverse identification method.

In all the works cited in the literature, the viscoelastic behavior of the resin is readily accessible. In the present work, an inverse method is presented to identify simultaneously the viscoelastic behavior of the resin, of the yarns and of the woven composite from only in-plane measurements on the composite. A two-stage finite element homogenization method has been used, with Periodic Boundary Conditions (PBCs). In order to apply a uniaxial tension along the $45°$ direction on the unit cell of the composite, additional developments to the PBCs are necessary and presented in Appendix B.

With the inverse method, a very good agreement is found between experimental and numerical results for the three orientations $0°$, $45°$ and $90°$, assuming that different types of glass fibers are used in warp and fill directions. The difference in glass material has been confirmed by nanoindentation measurements on fibers. A second outcome of the inverse method is the viscoelastic behavior of the resin. Resin samples are obtained from B-stage pre-impregnated laminates and subjected to relaxation tests. The resin response captured by the inverse method is consistent with the experimental one.

Finally, the identified behaviors of the resin and the composite are employed in the simulation of a buried via in a PCB configuration under temperature loads. The effects of different heating rates, hold times and maximum temperature are assessed. It has been shown that for a temperature excursion sufficiently below T_g, considering a thermo-elastic behavior for resin and laminate is a valid assumption. However, close to or above the T_g, it is necessary to use a viscoelastic constitutive behavior to expect predictive results in future works.

The identified viscoelastic response can be adopted to predict the stress distribution and reliability of PCBs in harsh environments. As an example, PCBs for e-mobility may contain active components which can generate large temperature loads, where important relaxation effects are expected. It is now also possible to investigate in more details crucial process operations accompanied with large temperature excursion like reflow soldering, associated with fast temperature increase above T_g. For all these conditions, the present work opens new possibilities, which will be explored in subsequent work.

Acknowledgments

The financial support of Eurométropole de Metz and Département de la Moselle is acknowledged as well as those of CIMULEC, SYSTRONIC and CSI SUD OUEST through the foundation ID+ Lorraine. G. Girard thanks the support of ANR through the project EMICI ANR-21-CE08-0007. The authors acknowledge the experimental facilities MécaRhéo from LEM3 (Université de Lorraine - CNRS UMR 7239).

Appendix A. Application of the Runge-Kutta method to the incremental formulation of history variables

The implicit Runge-Kutta Radau IIA method possesses excellent stability and convergence properties [41]. It also presents the advantage of only needing the function values at the previous time step (compared to other high order schemes requiring several time steps storage). These reasons make it an appropriate method for use in finite element schemes.

For implicit Runge-Kutta methods [42, 43, 44], the incremental solution to the differential equation

$$\frac{dy}{dt} = f(t, y) \tag{A.1}$$

takes the form

$$y_{n+1} = y_n + h \sum_{i=1}^{s} b_i k_i \tag{A.2}$$

with

$$k_i = f\left(t_n + c_i h, y_n + h \sum_{j=1}^{s} a_{ij} k_j\right) \tag{A.3}$$

In the above relations, h is the step size (denoted dt next), s the stage value. Values for a_{ij}, b_i, c_i for the Radau IIA method with $s = 3$ are provided by the Butcher tableau, see Table A.7. The index n corresponds to the current computation time step and $n + 1$ refers to the next step.

This method is applied to solve the differential equation for $\boldsymbol{q_k}$, in equation (20) (the index k is omitted in the following for the sake of simplicity):

$$\frac{\boldsymbol{dq}}{dt} = \frac{\boldsymbol{d\varepsilon}}{dt} - \frac{1}{\tau}\boldsymbol{q} \tag{A.4}$$

$\frac{2}{5} - \frac{\sqrt{6}}{10}$	$\frac{11}{45} - \frac{7\sqrt{6}}{360}$	$\frac{37}{225} - \frac{169\sqrt{6}}{1800}$	$-\frac{2}{225} + \frac{\sqrt{6}}{75}$
$\frac{2}{5} + \frac{\sqrt{6}}{10}$	$\frac{37}{225} + \frac{169\sqrt{6}}{1800}$	$\frac{11}{45} + \frac{7\sqrt{6}}{360}$	$-\frac{2}{225} - \frac{\sqrt{6}}{75}$
1	$\frac{4}{9} - \frac{\sqrt{6}}{36}$	$\frac{4}{9} + \frac{\sqrt{6}}{36}$	$\frac{1}{9}$
	$\frac{4}{9} - \frac{\sqrt{6}}{36}$	$\frac{4}{9} + \frac{\sqrt{6}}{36}$	$\frac{1}{9}$

Table A.7: Butcher tableau. The weights b_i are found on the bottom line, the nodes c_i are displayed in the left column and the coefficients a_{ij} fill the top right part of the tableau.

For Runge-Kutta Radau IIA with $s = 3$, a system of three equations for the k_i coefficients from equation (A.3) is obtained:

$$k_1 = \frac{\boldsymbol{d\varepsilon}}{dt} - \frac{1}{\tau}\left[\boldsymbol{q^n} + dt(a_{11}k_1 + a_{12}k_2 + a_{13}k_3)\right] \quad \text{(A.5)}$$

$$k_2 = \frac{\boldsymbol{d\varepsilon}}{dt} - \frac{1}{\tau}\left[\boldsymbol{q^n} + dt(a_{21}k_1 + a_{22}k_2 + a_{23}k_3)\right] \quad \text{(A.6)}$$

$$k_3 = \frac{\boldsymbol{d\varepsilon}}{dt} - \frac{1}{\tau}\left[\boldsymbol{q^n} + dt(a_{31}k_1 + a_{32}k_2 + a_{33}k_3)\right] \quad \text{(A.7)}$$

After solving this system for k_1, k_2 and k_3 and inserting them into equation (A.2), we finally get:

$$\boldsymbol{q^{n+1}} = a^{RK}\boldsymbol{d\varepsilon} + b^{RK}\boldsymbol{q^n} \quad \text{(A.8)}$$

with

$$a^{RK} = \frac{\tau(dt^2 + 6dt\tau + 60\tau^2)}{dt^3 + 9dt^2\tau + 36dt\tau^2 + 60\tau^3} \quad \text{(A.9)}$$

$$b^{RK} = \frac{\tau(3dt^2 - 24dt\tau + 60\tau^2)}{dt^3 + 9dt^2\tau + 36dt\tau^2 + 60\tau^3} \quad \text{(A.10)}$$

The history variables $\boldsymbol{q_k}$ can thus be updated for the new step (index $n+1$) from their previous values, the time step dt, the strain increment $\boldsymbol{d\varepsilon}$ and the relaxation times τ_k. Finally, the stress tensor $\boldsymbol{\sigma}$ is computed with equation (5).

In the present paper, an anisotropic linear viscoelastic material is considered. Such behavior is not available in the finite element software Abaqus. Therefore a subroutine UMAT has been written, implementing the above developments to update the stress tensor $\boldsymbol{\sigma}$ and history variables $\boldsymbol{q}$ from a given strain increment $\boldsymbol{d\varepsilon}$. It is also necessary to compute the Jacobian matrix. From equation (5), the expression of $\boldsymbol{d\sigma}$ is found:

$$\boldsymbol{d\sigma} = \underline{\boldsymbol{C_\infty}} : \boldsymbol{d\varepsilon} + \sum_{k=1}^{N} \underline{\boldsymbol{C_k}} : \boldsymbol{dq_k} \quad \text{(A.11)}$$

From equation (A.8), $\boldsymbol{dq_k}$ is evaluated:

$$\boldsymbol{dq_k} = \boldsymbol{q_k^{n+1}} - \boldsymbol{q_k^n} = a_k^{RK}\boldsymbol{d\varepsilon} + (b_k^{RK} - 1)\boldsymbol{q_k^n} \quad \text{(A.12)}$$

The Jacobian matrix can be readily obtained:

$$\frac{\partial \boldsymbol{d\sigma}}{\partial \boldsymbol{d\varepsilon}} = \underline{\boldsymbol{C_\infty}} + \sum_{k=1}^{N} \underline{\boldsymbol{C_k}} a_k^{RK} \quad \text{(A.13)}$$

The validity of the UMAT subroutine developed for the present work has been checked in comparison with the Abaqus implementation of the linear isotropic viscoelastic behavior with Prony series. The material is described by $E_0 = 12\,\text{GPa}$, $\nu_0 = 0.25$, a dimensionless bulk relaxation modulus $k = 0.4$, a dimensionless shear relaxation modulus $g = 0.4$, associated to a unique relaxation time $\tau = 1000\,\text{s}$. Two loading cases are considered: uniaxial tension (Figure A.20a) and shear (Figure A.20b). In both cases, a constant strain of $1\,\%$ is applied for $10\,000\,\text{s}$ followed by a zero load during $10\,000\,\text{s}$. The response obtained with the UMAT subroutine, using an isotropic behavior is identical to the one provided by Abaqus.

Appendix B. Periodic boundary conditions applied to a RVE subjected to uniaxial tension in an arbitrary direction.

Appendix B.1. General principle in 2D case

In 2D, Periodic Boundary Conditions (PBCs) on a rectangular unit cell are applied by controlling the displacements on the frontiers in a specific way [45, 46, 47]. The following relations describe the displacements on opposite sides of the RVE:

$$\begin{aligned} \bar{u}(0, x_2) - \bar{u}(l_1, x_2) &= \bar{U}1 \\ \bar{u}(x_1, 0) - \bar{u}(x_1, l_2) &= \bar{U}2 \end{aligned} \quad \text{(B.1)}$$

with l_1 and l_2 the dimensions of the unit cell, x_1 and x_2 are the coordinates of any material point on the remote boundary of the RVE. $\bar{U}1$ and $\bar{U}2$ describe the relative displacements between the two coincident points on opposite sides. The PBCs can therefore be implemented in a FE software by using two reference points to which the displacements $\bar{U}1$ and $\bar{U}2$ are assigned. The displacements of each pair of points on opposite sides must satisfy equation (B.1). When the unit cell is subjected to a 2D strain tensor $\boldsymbol{\varepsilon}$, the displacements $\bar{U}1$ and $\bar{U}2$ are expressed as:

$$\bar{U}1 = \begin{Bmatrix} \varepsilon_{11} \cdot l_1 \\ \varepsilon_{21} \cdot l_1 \end{Bmatrix}, \quad \bar{U}2 = \begin{Bmatrix} \varepsilon_{12} \cdot l_2 \\ \varepsilon_{22} \cdot l_2 \end{Bmatrix}, \quad \text{(B.2)}$$

where $\varepsilon_{12} = \varepsilon_{21}$. Note that when the unit cell is subjected to the displacement gradient (non symmetric tensor), one can also adopt relations (B.2) replacing the strain tensor by the displacement gradient.

By imposing the components of $\bar{U}1$ and $\bar{U}2$, it is possible to apply any overall loading for which the strain tensor is fully known. It is also possible to prescribe a uniaxial tension along one of the axes of the coordinate system (x_1, x_2) by specifying only one component of the strain tensor. The other components will be computed to satisfy equilibrium.

However, imposing a uniaxial tension in any arbitrary direction (different from the unit cell directions) is not straightforward. In the present work, it is necessary to impose uniaxial tension in a $45°$ direction for the inverse method of section 4.2.3. One could think to use a unit cell oriented in the chosen direction, but in the general case (arbitrary values for l_1 and l_2) or for an arbitrary direction, finding a periodic unit cell can be

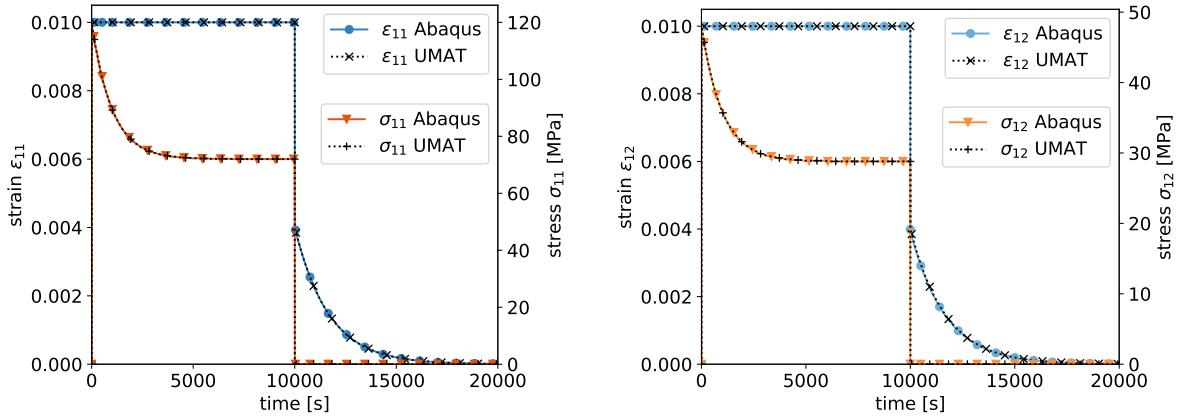

(a) (b)

Figure A.20: Validation of the numerical implementation of the viscoelastic behavior via the UMAT subroutine. (a) Tensile and (b) shear response of an element subjected to a constant strain followed by zero load.

impossible (see Figure B.21 for illustration). We propose therefore a methodology to keep the unit cell and the PBCs in the original coordinate system (x_1, x_2), while uniaxial tension (or any other strain loading) is applied in the transformed coordinate system (x_1^*, x_2^*), rotated by an angle θ.

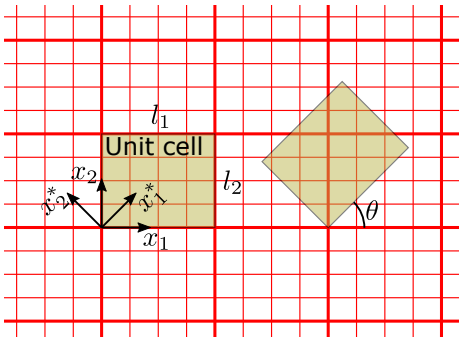

Figure B.21: Illustration of a unit cell in a periodic medium. In general, rotating the frame of the unit cell does not lead to a periodic unit cell, as seen on the right of the figure. Finding a periodic unit cell in an arbitrary direction may require a much larger unit cell or can even be impossible. Therefore the choice is made to use the original unit cell and PBCs in the coordinate system of the medium (x_1, x_2), while the loading is applied in the transformed coordinate system (x_1^*, x_2^*).

In the transformed basis, the strain tensor associated to a uniaxial tension writes:

$$\boldsymbol{\varepsilon^*} = \begin{bmatrix} \varepsilon_{11}^{*,kn} & \varepsilon_{12}^{*,un} \\ \varepsilon_{21}^{*,un} & \varepsilon_{22}^{*,un} \end{bmatrix}, \tag{B.3}$$

where superscripts kn and un denote known and unknown quantities. In the original coordinate system, the strain writes:

$$\boldsymbol{\varepsilon} = \boldsymbol{R\varepsilon^* R^T}, \tag{B.4}$$

With R the transformation matrix, expressed as (for a rotation θ around the third axis):

$$\boldsymbol{R} = \begin{bmatrix} cos(\theta) & -sin(\theta) \\ sin(\theta) & cos(\theta) \end{bmatrix}. \tag{B.5}$$

Finally, the RVE is subjected to the following strain tensor in the original coordinate system:

$$\boldsymbol{\varepsilon} = \begin{bmatrix} c^2\varepsilon_{11}^{*,kn} - cs\varepsilon_{12}^{*,un} - cs\varepsilon_{21}^{*,un} + s^2\varepsilon_{22}^{*,un} & cs\varepsilon_{11}^{*,kn} + c^2\varepsilon_{12}^{*,un} - s^2\varepsilon \\ cs\varepsilon_{11}^{*,kn} - s^2\varepsilon_{12}^{*,un} + c^2\varepsilon_{21}^{*,un} - cs\varepsilon_{22}^{*,un} & s^2\varepsilon_{11}^{*,kn} + cs\varepsilon_{12}^{*,un} + cs\varepsilon \end{bmatrix} \tag{B.6}$$

where c and s denote respectively $cos(\theta)$ and $sin(\theta)$. Each component of the strain tensor is unknown, resulting in the impossibility to apply the expected loading. The same reasoning is applicable to any loading containing one or several unknowns in a transformed coordinate system, in two or in three dimensions.

To overcome the above difficulties, we propose to define additional reference points which will enable to apply a uniaxial loading in an arbitrary direction by keeping the PBCs in the original coordinate system. The additional reference points control the displacements applied to the unit cell in the transformed coordinate system :

$$\bar{U1}^* = \begin{Bmatrix} \varepsilon_{11}^* \cdot l_1 \\ \varepsilon_{21}^* \cdot l_1 \end{Bmatrix}, \quad \bar{U2}^* = \begin{Bmatrix} \varepsilon_{12}^* \cdot l_2 \\ \varepsilon_{22}^* \cdot l_2 \end{Bmatrix} \tag{B.7}$$

Equation (B.6) can be written in the form:

$$\begin{Bmatrix} \varepsilon_{11} \\ \varepsilon_{12} \\ \varepsilon_{21} \\ \varepsilon_{22} \end{Bmatrix} = \begin{bmatrix} c^2 & -cs & -cs & s^2 \\ cs & c^2 & -s^2 & -cs \\ cs & -s^2 & c^2 & -cs \\ s^2 & cs & cs & c^2 \end{bmatrix} \begin{Bmatrix} \varepsilon_{11}^* \\ \varepsilon_{12}^* \\ \varepsilon_{21}^* \\ \varepsilon_{22}^* \end{Bmatrix} \tag{B.8}$$

The displacements $\bar{U1}^*$ and $\bar{U2}^*$ can be related to $\bar{U1}$ and $\bar{U2}$ by using equations (B.2), (B.7) and (B.8):

$$U1_1 = c^2 U1_1^* - \frac{l_1}{l_2} csU2_1^* - csU1_2^* + \frac{l_1}{l_2} s^2 U2_2^* \tag{B.9}$$

$$U2_1 = \frac{l_2}{l_1} csU1_1^* + c^2 U2_1^* - \frac{l_2}{l_1} s^2 U1_2^* - csU2_2^* \tag{B.10}$$

$$U1_2 = csU1_1^* - \frac{l_1}{l_2} s^2 U2_1^* + c^2 U1_2^* - \frac{l_1}{l_2} csU2_2^* \tag{B.11}$$

$$U2_2 = \frac{l_2}{l_1} s^2 U1_1^* + csU2_1^* + \frac{l_2}{l_1} csU1_2^* + c^2 U2_2^* \qquad \text{(B.12)}$$

The two additional reference points and the above four relations allow for the application of any overall strain state in any desired direction to the unit cell. For example, to apply a uniaxial strain in the direction θ, only $\bar{U1}_1^*$ is specified. The other components of the displacement of the reference points are computed by the solver to satisfy the equilibrium equations.

Appendix B.2. 3D generalization of PBCs for general loading

Applying the method in the 3D case can be achieved by following the same steps as in 2D case. The number of components is more important because of the additional degrees of freedom. In 3D, three reference points are needed to apply PBCs. The displacements assigned to the reference points are:

$$\bar{U1} = \begin{Bmatrix} \varepsilon_{11} \cdot l_1 \\ \varepsilon_{21} \cdot l_1 \\ \varepsilon_{31} \cdot l_1 \end{Bmatrix}, \quad \bar{U2} = \begin{Bmatrix} \varepsilon_{12} \cdot l_2 \\ \varepsilon_{22} \cdot l_2 \\ \varepsilon_{32} \cdot l_2 \end{Bmatrix}, \quad \bar{U3} = \begin{Bmatrix} \varepsilon_{13} \cdot l_3 \\ \varepsilon_{23} \cdot l_3 \\ \varepsilon_{33} \cdot l_3 \end{Bmatrix}, \qquad \text{(B.13)}$$

with l_1, l_2 and l_3 the dimensions of the unit cell in directions 1, 2 and 3 respectively. Three additional reference points are used to carry the displacements in the transformed frame:

$$\bar{U1}^* = \begin{Bmatrix} \varepsilon_{11}^* \cdot l_1 \\ \varepsilon_{21}^* \cdot l_1 \\ \varepsilon_{31}^* \cdot l_1 \end{Bmatrix}, \quad \bar{U2}^* = \begin{Bmatrix} \varepsilon_{12}^* \cdot l_2 \\ \varepsilon_{22}^* \cdot l_2 \\ \varepsilon_{32}^* \cdot l_2 \end{Bmatrix}, \quad \bar{U3}^* = \begin{Bmatrix} \varepsilon_{13}^* \cdot l_3 \\ \varepsilon_{23}^* \cdot l_3 \\ \varepsilon_{33}^* \cdot l_3 \end{Bmatrix}. \qquad \text{(B.14)}$$

In 3D, the arbitrary direction of the rotated coordinate system can be defined by the Euler angles: a first rotation of angle α around the 3 axis ($\boldsymbol{R_\alpha}$), a second rotation of angle β around the new 1 axis ($\boldsymbol{R_\beta}$), and a third rotation of angle γ around the new 3 axis ($\boldsymbol{R_\gamma}$). The corresponding transformation matrix is computed as $\boldsymbol{R} = \boldsymbol{R_\alpha R_\beta R_\gamma}$.

The strain components in the original coordinate system are expressed as a function of the strain components in the transformed coordinate system: $\boldsymbol{\varepsilon} = \boldsymbol{R\varepsilon^* R^T}$.

$$\begin{Bmatrix} \varepsilon_{11} \\ \varepsilon_{12} \\ \varepsilon_{13} \\ \varepsilon_{21} \\ \varepsilon_{22} \\ \varepsilon_{23} \\ \varepsilon_{31} \\ \varepsilon_{32} \\ \varepsilon_{33} \end{Bmatrix} = \begin{bmatrix} k_{11} & k_{12} & k_{13} & k_{14} & k_{15} & k_{16} & k_{17} & k_{18} & k_{19} \\ k_{21} & k_{22} & k_{23} & k_{24} & k_{25} & k_{26} & k_{27} & k_{28} & k_{29} \\ k_{31} & k_{32} & k_{33} & k_{34} & k_{35} & k_{36} & k_{37} & k_{38} & k_{39} \\ k_{41} & k_{42} & k_{43} & k_{44} & k_{45} & k_{46} & k_{47} & k_{48} & k_{49} \\ k_{51} & k_{52} & k_{53} & k_{54} & k_{55} & k_{56} & k_{57} & k_{58} & k_{59} \\ k_{61} & k_{62} & k_{63} & k_{64} & k_{65} & k_{66} & k_{67} & k_{68} & k_{69} \\ k_{71} & k_{72} & k_{73} & k_{74} & k_{75} & k_{76} & k_{77} & k_{78} & k_{79} \\ k_{81} & k_{82} & k_{83} & k_{84} & k_{85} & k_{86} & k_{87} & k_{88} & k_{89} \\ k_{91} & k_{92} & k_{93} & k_{94} & k_{95} & k_{96} & k_{97} & k_{98} & k_{99} \end{bmatrix} \begin{Bmatrix} \varepsilon_{11}^* \\ \varepsilon_{12}^* \\ \varepsilon_{13}^* \\ \varepsilon_{21}^* \\ \varepsilon_{22}^* \\ \varepsilon_{23}^* \\ \varepsilon_{31}^* \\ \varepsilon_{32}^* \\ \varepsilon_{33}^* \end{Bmatrix} \qquad \text{(B.15)}$$

Relation (B.15) is also valid for non symmetric tensor, when displacement gradient is imposed to the unit cell, instead of a strain tensor. Expressions of components k_{ij} can be derived by simple algebra.

It is therefore possible to express the displacements $\bar{U1}$, $\bar{U2}$, $\bar{U3}$ of the three reference points in the original frame as a function of the displacements of the three reference points in the transformed frame $\bar{U1}^*$, $\bar{U2}^*$, $\bar{U3}^*$ with nine equations:

$$\begin{aligned}
U1_1 &= k_{11}U1_1^* + \frac{l_1}{l_2}k_{12}U2_1^* + \frac{l_1}{l_3}k_{13}U3_1^* \\
&\quad + k_{14}U1_2^* + \frac{l_1}{l_2}k_{15}U2_2^* + \frac{l_1}{l_3}k_{16}U3_2^* \\
&\quad + k_{17}U1_3^* + \frac{l_1}{l_2}k_{18}U2_3^* + \frac{l_1}{l_3}k_{19}U3_3^* \\
U2_1 &= \frac{l_2}{l_1}k_{21}U1_1^* + k_{22}U2_1^* + \frac{l_2}{l_3}k_{23}U3_1^* \\
&\quad + \frac{l_2}{l_1}k_{24}U1_2^* + k_{25}U2_2^* + \frac{l_2}{l_3}k_{26}U3_2^* \\
&\quad + \frac{l_2}{l_1}k_{27}U1_3^* + k_{28}U2_3^* + \frac{l_2}{l_3}k_{29}U3_3^* \\
U3_1 &= \frac{l_3}{l_1}k_{31}U1_1^* + \frac{l_3}{l_2}k_{32}U2_1^* + k_{33}U3_1^* \\
&\quad + \frac{l_3}{l_1}k_{34}U1_2^* + \frac{l_3}{l_2}k_{35}U2_2^* + k_{36}U3_2^* \\
&\quad + \frac{l_3}{l_1}k_{37}U1_3^* + \frac{l_3}{l_2}k_{38}U2_3^* + k_{39}U3_3^* \\
U1_2 &= k_{41}U1_1^* + \frac{l_1}{l_2}k_{42}U2_1^* + \frac{l_1}{l_3}k_{43}U3_1^* \\
&\quad + k_{44}U1_2^* + \frac{l_1}{l_2}k_{45}U2_2^* + \frac{l_1}{l_3}k_{46}U3_2^* \\
&\quad + k_{47}U1_3^* + \frac{l_1}{l_2}k_{48}U2_3^* + \frac{l_1}{l_3}k_{49}U3_3^* \\
U2_2 &= \frac{l_2}{l_1}k_{51}U1_1^* + k_{52}U2_1^* + \frac{l_2}{l_3}k_{53}U3_1^* \\
&\quad + \frac{l_2}{l_1}k_{54}U1_2^* + k_{55}U2_2^* + \frac{l_2}{l_3}k_{56}U3_2^* \\
&\quad + \frac{l_2}{l_1}k_{57}U1_3^* + k_{58}U2_3^* + \frac{l_2}{l_3}k_{59}U3_3^* \\
U3_2 &= \frac{l_3}{l_1}k_{61}U1_1^* + \frac{l_3}{l_2}k_{62}U2_1^* + k_{63}U3_1^* \\
&\quad + \frac{l_3}{l_1}k_{64}U1_2^* + \frac{l_3}{l_2}k_{65}U2_2^* + k_{66}U3_2^* \\
&\quad + \frac{l_3}{l_1}k_{67}U1_3^* + \frac{l_3}{l_2}k_{68}U2_3^* + k_{69}U3_3^* \\
U1_3 &= k_{71}U1_1^* + \frac{l_1}{l_2}k_{72}U2_1^* + \frac{l_1}{l_3}k_{73}U3_1^* \\
&\quad + k_{74}U1_2^* + \frac{l_1}{l_2}k_{75}U2_2^* + \frac{l_1}{l_3}k_{76}U3_2^* \\
&\quad + k_{77}U1_3^* + \frac{l_1}{l_2}k_{78}U2_3^* + \frac{l_1}{l_3}k_{79}U3_3^* \\
U2_3 &= \frac{l_2}{l_1}k_{81}U1_1^* + k_{82}U2_1^* + \frac{l_2}{l_3}k_{83}U3_1^* \\
&\quad + \frac{l_2}{l_1}k_{84}U1_2^* + k_{85}U2_2^* + \frac{l_2}{l_3}k_{86}U3_2^* \\
&\quad + \frac{l_2}{l_1}k_{87}U1_3^* + k_{88}U2_3^* + \frac{l_2}{l_3}k_{89}U3_3^* \\
U3_3 &= \frac{l_3}{l_1}k_{91}U1_1^* + \frac{l_3}{l_2}k_{92}U2_1^* + k_{93}U3_1^* \\
&\quad + \frac{l_3}{l_1}k_{94}U1_2^* + \frac{l_3}{l_2}k_{95}U2_2^* + k_{96}U3_2^* \\
&\quad + \frac{l_3}{l_1}k_{97}U1_3^* + \frac{l_3}{l_2}k_{98}U2_3^* + k_{99}U3_3^* \qquad \text{(B.16)}
\end{aligned}$$

By specifying the orientation of the transformed coodinate system and the desired strain components, it is possible to apply any overall strain tensor to the unit cell by the means of three additional reference points and nine equations connecting them to the reference points responsible for the PBCs. The present PBCs have been implemented in ABAQUS software and have been used to determine the viscoelastic response of the resin with recourse to the inverse method.

References

[1] A. Salahouelhadj, M. Martiny, S. Mercier, L. Bodin, D. Manteigas, B. Stephan, Reliability of thermally stressed rigid–flex printed circuit boards for high density interconnect applications, Microelectronics Reliability 54 (1) (2014) 204 – 213.

[2] K. Watanabe, Y. Kariya, N. Yajima, K. Obinata, Y. Hiroshima, S. Kikuchi, A. Matsui, H. Shimizu, Low-cycle fatigue testing and thermal fatigue life prediction of electroplated copper thin film for through hole via, Microelectronics Reliability 82 (2018) 20 – 27.

[3] W. Kpobie, M. Martiny, S. Mercier, F. Lechleiter, L. Bodin, Thermomechanical simulation of pcb with embedded components, Microelectronics Reliability 65 (2016) 108–130.

[4] E. J. Barbero, J. Trovillion, J. A. Mayugo, K. K. Sikkil, Finite element modeling of plain weave fabrics from photomicrograph measurements, Composite Structures 73 (2006) 41–52.

[5] S. D. Green, M. Y. Matveev, A. C. Long, D. Ivanov, S. R. Hallett, Mechanical modelling of 3d woven composites considering realistic unit cell geometry, Composite Structures 118 (2014) 284–293.

[6] Z. Chen, F. Yang, S. A. Meguid, Multi-level modeling of woven glass/epoxy composite for multilayer printed circuit board applications, International Journal of Solids and Structures 51 (2014) 3679–3688.

[7] G. Girard, M. Jrad, S. Bahi, M. Martiny, S. Mercier, L. Bodin, D. Nevo, S. Dareys, Experimental and numerical characterization of thin woven composites used in printed circuit boards for high frequency applications, Composite Structures 193 (2018) 140 – 153.

[8] Q. Zhu, P. Shrotriya, N. R. Sottos, P. H. Geubelle, Three-dimensional viscoelastic simulation of woven composite substrates for multilayer circuit boards, Composites science and technology 63 (13) (2003) 1971–1983.

[9] K. Kwok, S. Pellegrino, Micromechanics models for viscoelastic plain-weave composite tape springs, AIAA Journal 55 (1) (2017) 309–321.

[10] Y. Xu, P. Zhang, W. Zhang, Two-scale micromechanical modeling of the time dependent relaxation modulus of plain weave polymer matrix composites, Composite structures 123 (2015) 35–44.

[11] A. Courtois, M. Hirsekorn, M. Benavente, A. Jaillon, L. Marcin, E. Ruiz, M. Lévesque, Viscoelastic behavior of an epoxy resin during cure below the glass transition temperature: Characterization and modeling, Journal of Composite Materials 53 (2) (2019) 155–171.

[12] A. Courtois, L. Marcin, M. Benavente, E. Ruiz, M. Lévesque, Numerical multiscale homogenization approach for linearly viscoelastic 3d interlock woven composites, International Journal of Solids and Structures 163 (2019) 61–74.

[13] M. Benavente, L. Marcin, A. Courtois, M. Lévesque, E. Ruiz, Numerical analysis of viscoelastic process-induced residual distortions during manufacturing and post-curing, Composites Part A: Applied Science and Manufacturing 107 (2018) 205–216.

[14] Z. Hashin, The inelastic inclusion problem, International Journal of Engineering Science 7 (1) (1969) 11–36.

[15] M. Hirsekorn, L. Marcin, T. Godon, Multi-scale modeling of the viscoelastic behavior of 3d woven composites, Composites Part A: Applied Science and Manufacturing 112 (2018) 539–548.

[16] M. Hirsekorn, L. Marcin, T. Godon, Thermo-viscoelastic homogenization of 3d woven composites with time-dependent expansion coefficients, International Journal of Solids and Structures 244-245 (2022) 111569.

[17] R. Polanskỳ, V. Mentlík, P. Prosr, J. Sušír, Influence of thermal treatment on the glass transition temperature of thermosetting epoxy laminate, Polymer Testing 28 (4) (2009) 428–436.

[18] R. Polanskỳ, P. Prosr, M. Čermák, Determination of the thermal endurance of pcb fr4 epoxy laminates via thermal analyses, Polymer degradation and stability 105 (2014) 107–115.

[19] M. Lé-Magda, E. Dargent, J. A. S. Puente, A. Guillet, E. Font, J.-M. Saiter, Influence of very long aging on the relaxation behavior of flame-retardant printed circuit board epoxy composites under mechatronic conditions, Journal of Applied Polymer Science 130 (2) (2013) 786–792.

[20] M. Gigliotti, M. Minervino, M. Lafarie-Frenot, J. Grandidier, Effect of thermo-oxidation on the local mechanical behaviour of epoxy polymer materials for high temperature applications, Mechanics of Materials 101 (2016) 118–135.

[21] R. L. Taylor, K. S. Pister, G. L. Goudreau, Thermomechanical analysis of viscoelastic solids, International Journal for Numerical Methods in Engineering 2 (1) (1970) 45–59.

[22] H. F. Brinson, Mechanical and optical viscoelastic characterization of hysol 4290, Experimental Mechanics 8 (12) (1968) 561–566.

[23] C. Popelar, C. Popelar, V. Kenner, Viscoelastic material characterization and modeling for polyethylene, Polymer Engineering & Science 30 (10) (1990) 577–586.

[24] E. Woo, J. Seferis, R. Schaffnit, Viscoelastic characterization of high performance epoxy matrix composites, Polymer Composites 12 (4) (1991) 273–280.

[25] R. J. Thorpe, Experimental characterization of the viscoelastic behavior of a curing epoxy matrix composite from pre-gelation to full cure, Ph.D. thesis, University of British Columbia (2013).

[26] N. Zobeiry, R. Vaziri, A. Poursartip, Differential Implementation of the Viscoelastic Response of a Curing Thermoset Matrix for Composites Processing, Journal of Engineering Materials and Technology 128 (1) (2005) 90–95.

[27] T. Crochon, T. Schönherr, C. Li, M. Lévesque, On finite-element implementation strategies of schapery-type constitutive theories, Mechanics of Time-Dependent Materials 14 (4) (2010) 359–387.

[28] M. B. Miana, Viscoelastic distortion during manufacturing and post-curing of thermoset composites: Characterization and modeling, Ph.D. thesis, Ecole Polytechnique, Montreal (Canada) (2017).

[29] M. W. Nielsen, Predictions of process induced shape distortions and residual stresses in large fibre reinforced composite laminates, Ph.D. thesis, Technical University of Denmark, Department of Mechanical Engineering (2012).

[30] M. Machado, U. D. Cakmak, I. Kallai, Z. Major, Thermomechanical viscoelastic analysis of woven-reinforced thermoplastic-matrix composites, Composite Structures 157 (2016) 256–264.

[31] H. Poon, M. F. Ahmad, A finite element constitutive update scheme for anisotropic, viscoelastic solids exhibiting non-linearity of the schapery type, International Journal for Numerical Methods in Engineering 46 (12) (1999) 2027–2041.

[32] N. K. Naik, V. K. Ganesh, Prediction of on-axes elastic properties of plain weave fabric composites, Composites Science and Technology 45 (1992) 135–152.

[33] V. G. Martynenko, G. I. Lvov, Numerical prediction of temperature-dependent anisotropic viscoelastic properties of fiber reinforced composite, Journal of Reinforced Plastics and Composites 36 (24) (2017) 1790–1801.

[34] A. Atintoh, W. Kpobie, N. Bonfoh, M. Fendler, F. Addiego, P. Lipinski, Multiscale characterization of the mechanical behavior of a printed circuit board (PCB), Materials Today Communications 34 (2023) 104968.

[35] H. Li, J. C. Watson, Continuous glass fibers for reinforcement, Encyclopedia of Glass Science, Technology, History, and Culture 1 (2021) 95–109.

[36] R. A. Schapery, On the characterization of nonlinear viscoelastic materials, Polymer Engineering & Science 9 (4) (1969) 295–310.

[37] D. Qvale, K. Ravi-Chandar, Viscoelastic characterization of polymers under multiaxial compression, Mechanics of time-dependent materials 8 (2004) 193–214.

[38] N. W. Tschoegl, W. G. Knauss, I. Emri, Poisson's ratio in linear viscoelasticity–a critical review, Mechanics of Time-Dependent Materials 6 (2002) 3–51.

[39] W. C. Oliver, G. M. Pharr, An improved technique for determining hardness and elastic modulus using load and displacement sensing indentation experiments, Journal of materials research 7 (6) (1992) 1564–1583.

[40] G. Girard, M. Martiny, S. Mercier, Experimental characterization of rolled annealed copper film used in flexible printed circuit boards: Identification of the elastic-plastic and low-cycle fatigue behaviors, Microelectronics Reliability 115 (2020) 113976.

[41] S. González-Pinto, S. Pérez-Rodríguez, J. Montijano, Implementation of high-order implicit runge-kutta methods, Computers & Mathematics with Applications 41 (7) (2001) 1009–1024.
[42] G. Wanner, E. Hairer, Solving ordinary differential equations II, Vol. 375, Springer Berlin Heidelberg, 1996.
[43] J. C. Butcher, Implicit runge-kutta processes, Mathematics of Computation 18 (85) (1964) 50–64.
[44] J. Büttner, B. Simeon, Runge–kutta methods in elastoplasticity, Applied Numerical Mathematics 41 (4) (2002) 443–458.
[45] W. Tian, L. Qi, X. Chao, J. Liang, M. Fu, Periodic boundary condition and its numerical implementation algorithm for the evaluation of effective mechanical properties of the composites with complicated micro-structures, Composites Part B: Engineering 162 (2019) 1–10.
[46] O. Pierard, J. LLorca, J. Segurado, I. Doghri, Micromechanics of particle-reinforced elasto-viscoplastic composites: Finite element simulations versus affine homogenization, International Journal of Plasticity 23 (2007) 1041–1060.
[47] M. Herráez, C. González, C. S. Lopes, R. Guzmán de Villoria, J. LLorca, T. Varela, J. Sánchez, Computational micromechanics evaluation of the effect of fibre shape on the transverse strength of unidirectional composites: An approach to virtual materials design, Composites 91 (2016) 484–492.